CHINESE OPTICS LETTERS

Vol. 20, No. 11 | November 2022

Progress on photovoltaic AlGaN photodiodes for solar-blind ultraviolet photodetection

Xu Liu (刘 旭) and Shengjun Zhou (周圣军)*

Center for Photonics and Semiconductors, School of Power and Mechanical Engineering, Wuhan University, Wuhan 430072, China

*Corresponding author: zhousj@whu.edu.cn

Received March 17, 2022 | Accepted June 6, 2022 | Posted Online August 10, 2022

Solar-blind ultraviolet photodetectors (SBPDs) have attracted tremendous attention in the environmental, industrial, military, and biological fields. Aluminum gallium nitride (AlGaN), a kind of representative III-nitride semiconductor, has promising prospects in solar-blind photodetection owing to its tunable wide bandgap and industrial feasibility. Considering the high defect density in the AlGaN epilayer directly grown on a sapphire substrate, employing an AlN/sapphire template turns out to be an effective method to achieve a high-quality AlGaN epilayer, thereby enhancing the SBPD performances. In recent years, a variety of remarkable breakthroughs have been achieved in the SBPDs. In this paper, the progress on photovoltaic AlGaN-based SBPDs is reviewed. First, the basic physical properties of AlGaN are introduced. Then, fabrication methods and defect annihilation of the AlN/sapphire template are discussed. Various photovoltaic SBPDs are further summarized, including Schottky barrier, metal-semiconductor-metal, p-n/p-i-n and avalanche photodiodes. Furthermore, surface modification and photoelectrochemical cell techniques are introduced. Benefitting from the development of fabrication techniques and optoelectronic devices, photovoltaic AlGaN photodiodes exhibit a promising prospect in solar-blind ultraviolet photodetection.

Keywords: photovoltaic AlGaN photodiodes; solar-blind ultraviolet photodetection; AlN/sapphire template.

DOI: 10.3788/COL202220.112501

1. Introduction

Ultraviolet (UV) light accounts for 10% of the total solar spectrum. Based on the wavelength of UV light, the whole radiation region is divided into the four subregions: UVA (400–320 nm), UVB (320–280 nm), UVC (280–100 nm), and extreme UV (EUV) (120–10 nm)[1,2]. Among the four UV radiation subregions, UVC light can be entirely absorbed by the stratospheric ozone layer when sunlight penetrates through the atmosphere so that there are no UVC photons naturally existing in Earth's atmosphere. Therefore, the UVC radiation light is also called solar-blind UV light. The feature ensures that the background noise can be maximally screened during solar-blind photodetection, which offers potential applications in early missile threat warning and tracking, environmental monitoring, engine monitoring, flame detection, and non-line-of-sight communications[3–5].

III-nitride semiconductors, including GaN, AlN, InN, and their ternary (AlGaN, InGaN) and quaternary alloys (AlGaInN), exhibit superior properties, such as a wide energy bandgap, large thermal conductivity, high carrier mobility, strong anti-radiation ability, and good chemical stability[6]. Among these III-nitride semiconductors, AlGaN alloys have adjustable bandgaps in the range from 3.4 to 6.2 eV by changing the Al content. When the Al content is larger than 0.4, the $Al_xGa_{1-x}N$ alloys will exhibit the ability of solar-blind photodetection. In addition, AlGaN alloys have many merits, including good mechanical strength, high breakdown field, strong thermal stability, etc. Therefore, AlGaN alloys are suitable for UV photodetectors, light-emitting diodes (LEDs), laser diodes, high-speed electronics devices, and high-frequency transistors operated under extreme conditions[7,8].

According to the operation mode, solar-blind ultraviolet photodetectors (SBPDs) are generally divided into photoconductive SBPDs and photovoltaic SBPDs. Photoconductive SBPDs have been investigated in the past several decades. Their photodetection behavior is based on the fact that the electrical conductivity of SBPDs will change when exposed to the radiation of solar-blind UV light. Photoconductive SBPDs are fit for mass production. However, they also suffer from several fatal drawbacks, including slow response speed, low-energy photon response, and severe temperature dependence. Photovoltaic SBPDs are those photodetectors whose work mechanism is based on the photovoltaic effect. The electric field resulting from the photovoltaic effect at the interfaces can facilitate the separation and transport of photogenerated carriers, thereby resulting in enhanced responsivity and response speed of photovoltaic SBPDs. There are several configurations of photovoltaic photodiodes used for solar-blind UV photodetection, including p-n/p-i-n, Schottky barrier, metal-semiconductor-metal (MSM), and avalanche photodiodes (APDs). In recent years, photovoltaic AlGaN photodiodes have been rapidly developed, which is important for the development of high-performance SBPDs.

In this review, we summarize recent development of photovoltaic AlGaN SBPDs. First, we focus on the AlGaN epilayers and low-defect AlN/sapphire template. Then, we discuss several types of photovoltaic AlGaN SBPDs, including device configurations, performance improvement methods, and physical mechanisms. Moreover, the advances in photovoltaic AlGaN SBPDs are reviewed to better understand solar-blind UV photodetection technology for versatile applications.

2. AlGaN Materials

The crystalline quality of AlGaN alloys exerts a strong influence on the detection performance of AlGaN SBPDs. This section is focused on the fabrication methods of AlGaN epitaxial films and their corresponding template techniques.

2.1. AlGaN epitaxial films

Three methods are mainly used to grow the AlGaN absorption layers, including liquid phase epitaxy (LPE), molecular beam epitaxy (MBE), and vapor phase epitaxy (VPE)[9–11]. LPE is the most low-cost among the above-mentioned methods. Nevertheless, it is no longer adaptive to fabricating high-performance SBPDs because the thickness of achieving an epilayer is limited via using LPE. In addition, the gradient of impurity concentrations and the type of conductivity are not easy to change intentionally during growth. MBE can be used to accurately control the thickness of the epilayers under a lower temperature in comparison to VPE and LPE. However, the slow growth rate and complex equipment obstruct the large-scale production. Hydride VPE (HVPE) is also a method that can be used to rapidly grow AlGaN films[12,13]. Like LPE, HVPE cannot precisely control the thickness of the AlGaN films. In addition, the reaction gas used during the growth process can also corrode the equipment, which may exert serious influence on the purity of AlGaN materials. Metal-organic VPE (MOVPE) can accurately control the film thickness with a moderate growth rate, which is particularly suitable for large-scale industrial production[14,15]. Therefore, MOVPE is the most widely used to fabricate AlGaN absorption layers for high-performance SBPDs. The typical AlGaN epitaxial film grown on the AlN/sapphire template is exhibited in Figs. 1(a)–1(c)[16].

2.2. Van der Waals epitaxy of AlN template

Van der Waals epitaxy (vdWE) is quite different from conventional epitaxy owing to the noncovalent bond between the epitaxial material and the substrate at the interface. Although the orientation relationship of the epitaxial material is consistent

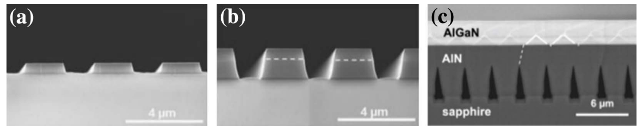

Fig. 1. Cross-section SEM images of (a) stripe-shaped PSS, (b) AlN/PSS template, and (c) AlGaN epitaxial film grown on AlN/PSS template. Reproduced with permission[16]. Copyright 2013, Elsevier.

with the substrate, lattice match is not important for vdWE, which is called incommensurate epitaxy; the in-plane lattice parameters of the three-dimensional (3D) materials will be very close to the bulk value, resulting in no excessive strain and dislocation originating from the lattice mismatch. Recently, AlN vdWE technology has drawn much scientific interest[17,18]. Chang *et al*. reported achieving of high-quality AlN epitaxial film on nano-patterned sapphire substrate (NPSS) via graphene-assisted quasi-vdWE (QvdWE) in Fig. 2[17]. It is found that the growth of AlN follows the 3D longitudinal island growth mode, and the lateral coalescence of the AlN nucleation islands is relatively slow, which makes it hard to cover the NPSS at a thin growth thickness. Due to Gr, Al atoms can laterally migrate more easily on the Gr layer than on the bare NPSS, which is beneficial for the two-dimensional (2D) growth mode of AlN, thereby resulting in rapid and lateral coalescence with a thin and flat AlN film. The obtained AlN by using QvdWE exhibited a reduced dislocation density. It is found that a 2.6-time increase in electroluminescence (EL) intensity was realized in deep

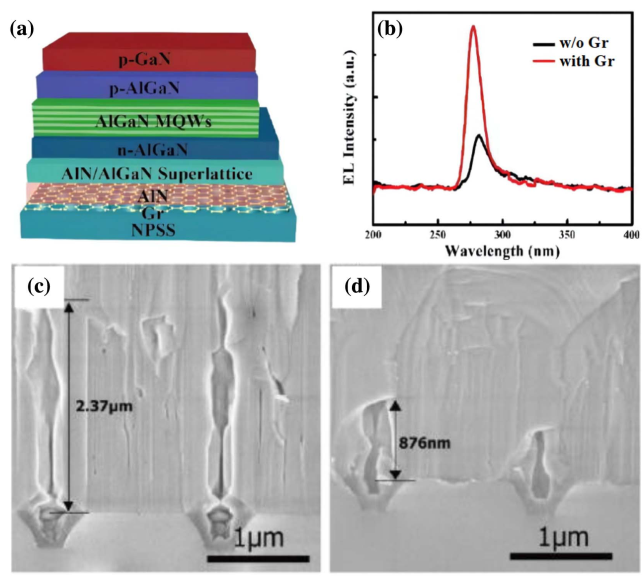

Fig. 2. (a) Schematic diagram of the DUV LED grown on AlN/Gr/NPSS. (b) EL spectra of the DUV-LEDs with and without the Gr interlayer. Cross-sectional SEM images of AlN films on NPSS (c) without and (d) with the Gr interlayer. AlN has realized complete coalescence below a thickness of 1 μm in (d), which is less than half of the thickness (about 2.4 μm) on bare NPSS in (c). Reproduced with permission[17]. Copyright 2019, American Institute of Physics Publishing.

ultraviolet LEDs (DUV-LEDs) grown on Gr/NPSS in comparison to the DUV-LEDs grown on bare NPSS, as shown in Fig. 2(b).

2.3. Bulk AlN template

Bulk AlN is anticipated to act as a promising transparent substrate material for nitride devices because of the high thermal conductivity of up to 2.85 W/(cm K). The crystal quality of AlGaN grown on a bulk AlN substrate is intrinsically expected to be good because they both have the same crystallographic symmetry of wurtzite. Therefore, the use of the bulk AlN substrate during the photodetectors manufacturing is worth investigation[19–25]. For example, Jeong *et al.* reported top-illuminated $Al_{0.6}Ga_{0.4}N$ p-i-n SBPDs grown on an AlN bulk substrate and on another two types of AlN templates with different quality[19]. They found that the peak of the AlGaN SBPD grown on the AlN bulk substrate has a narrower linewidth compared to those of the AlGaN SBPDs grown on the AlN/sapphire templates in X-ray diffraction-based reciprocal space mapping. In addition, the surface roughness of the SBPD grown on the bulk AlN substrate is nearly 20 times lower than that of the SBPDs grown on AlN templates. As a result, the AlGaN SBPD grown on the bulk AlN substrate exhibited the lowest leakage current density of less than $1 \times 10^{-8}\ \mathrm{A/cm^2}$ in comparison to that of SBPDs grown on AlN templates at low reverse bias. This achievement can be attributed to high crystalline quality of the AlGaN epitaxial structure resulting from the application of a bulk AlN substrate.

2.4. AlN/sapphire template

Due to large lattice mismatch between the AlGaN and sapphire substrate, there are a vast number of dislocations and point defects existing in the AlGaN epilayers deposited on sapphire substrates. The high-density defects in AlGaN usually act as the non-radiative recombination centers, the carrier scattering centers, and the leakage current channels. The growth of high-quality AlGaN film is the key factor for obtaining high performance SBPDs[26–28]. Several reported AlN/sapphire templates are summarized in Table 1.

Bulk AlN substrates could be good candidates to achieve high-responsivity SBPD due to small lattice mismatch with the epitaxial layers and low dislocation density below $5 \times 10^8\ \mathrm{cm^{-2}}$, but they suffer from high-impurity absorption, high cost, and limited availability. It has already been proved that introduction of high-quality AlN/sapphire templates, including flat sapphire substrate (FSS)/patterned sapphire substrate (PSS), nano-scale-thick AlN nucleation layers (NLs), and micro-scale-thick AlN epitaxial films, is the foundation for high-quality AlGaN epilayers[36–41]. However, large lattice mismatch existing at the AlN/sapphire interface will result in numerous dislocations formed between the AlN and sapphire interface. Dislocation density in the AlN film normally ranges from 10^{10} to $10^{12}\ \mathrm{cm^{-2}}$, leading to relatively poor optoelectronic properties of SBPDs. To obtain a high-quality AlN/sapphire template, several growth techniques have been investigated, including epitaxial lateral overgrowth (ELOG) technology, pendeo-epitaxy, and facet-controlled ELOG[42,43]. Employing a low-temperature (LT) GaN or AlN buffer layer is an important method to diminish the lattice mismatch between the epilayers and sapphire substrate[44–47]. Our group found that densities of both screw dislocations and edge dislocations in the GaN epilayer grown on a PSS were much less than that of the GaN epilayer grown on an FSS[48]. The calculated densities of screw and edge dislocation were $1.29 \times 10^8\ \mathrm{cm^{-2}}$ and $4.1 \times 10^8\ \mathrm{cm^{-2}}$ for GaN grown on PSS.

Another method is to take the advantage of the NL[49,50]. We fabricated a series of UV LEDs grown on *ex-situ* sputtered-AlN NL/PSS, *in-situ* LT-GaN NL/PSS, and LT-AlGaN NL/PSS[51]. The light output power (LOP) of the UV LED on *ex-situ* sputtered AlN NL/PSS was higher than that of the UV LEDs on *in-situ* LT-AlGaN NL/PSS and LT-AlGaN NL/PSS. That was mainly attributed to the reduced threading dislocation density (TDD) in epitaxial films on *ex-situ* sputtered AlN NL/PSS. However, the above-discussed strategy is applied in the fabrication of UV LEDs. Nevertheless, the intrinsic logic of defect termination can also be used to fabricate high-performance photodetectors[52–54]. For example, Chang *et al.* reported two types of GaN-based Schottky barrier photodetectors that are grown on GaN NL/PSS and GaN NL/FSS templates[53]. Compared to the GaN photodetector grown on GaN NL/FSS, the GaN photodetector grown on GaN NL/PSS exhibited a reduced dark current and enhanced responsivity. In addition, noise equivalent power and normalized detectivity of the GaN photodetector grown on GaN NL/PSS were both higher than that of the GaN photodetector grown on GaN NL/FSS because of the high quality of the photodetector epitaxial structure resulting from the introduction of NL/PSS. This presented the advantages of NL/PSS in the fabrication of the photodetector.

High temperature annealing (HTA) can reduce dislocation densities by relaxing tensile stress, rearranging the AlN lattice, and facilitating generation of a new interface that has little influence on the lattice constant above/below this interface[55–57]. But, too high temperature will also deform the AlN/sapphire interface. Therefore, it is important that the annealing duration or temperature must be low enough. Several two-step approaches were reported for solving the problems[58–60]. For example, Hagedorn *et al.* found that AlN epitaxial films were formed at 1250°C via using MOVPE and then annealed at 1730°C for 1 h, which not only stabilized the AlN/sapphire interface but also reduced TDD during annealing[58]. Then, the AlN films subsequently were annealed at 1690°C for 3 h to further reduce TDD. As a result, TDD was first decreased to $3.5 \times 10^8\ \mathrm{cm^{-2}}$ after the first HTA and subsequently decreased to $2.5 \times 10^8\ \mathrm{cm^{-2}}$ after the second HTA.

Nucleation conditions of NLs are crucial for acquisition of low-defect-density AlN epitaxial films[61–64]. Balaji *et al.* investigated the effect of NL nucleation temperature on the crystalline quality of AlN epitaxial films in Fig. 3[65]. They deposited three NLs at 950°C, 1050°C, and 1150°C and recrystallized them at

Table 1. Summary of the Reported AlN/Sapphire Template.

Template	Thickness (μm)	Nucleation Layer	Defect Density[a] (cm^{-2})	Highlights	Ref.
AlN/MPSS	10.6	LT-AlN	Total: 3×10^8	1. PALE-induced[b] and ELOG-induced voids are both introduced in the AlN epilayer during growth.	[29]
			S: 5.9×10^7	2. These voids facilitate the defect termination and strain release in the AlN epilayer.	
			E: 2.3×10^8		
AlN/FSS	6	LT-AlN	TD: $< 10^8$	1. The nanoscale ELOG is achieved on the AlN rods/FSS template.	[30]
			S: 3.5×10^8	2. The advantage of the nanoscale ELOG is that even the dislocations in the center of the rod do not have a long distance to bend into the voids between the rods.	
			E: None	3. TDs bend at slight angles due to the nano-scaled air gaps and the rod diameters by nano-ELOG.	
AlN/MPSS	2.54	–	Total: 1×10^8	1. The effect of PSS on reducing defect density is investigated.	[31]
			EP: 2.3×10^5	2. AlN layers with gradient V/III ratio and period AlN superlattice layers (SLs) are introduced into the AlN epilayer to reduce defect density.	
				3. The behaviors of defect termination are exhibited quantitatively.	
AlN/NPSS	3.25	LT-AlN	TD: 1×10^9	The intrinsic mechanism of bending dislocations by employing AlN SLs with period high/low V/III ratio is revealed in Fig. 4.	[32]
AlN/FSS	2	Sputtered AlN LT-AlN	EP: 4.8×10^7	1. The effect of AlN NL thickness on optical transmittance, strain state, surface morphology, and TD density of AlN epilayer is investigated.	[14]
				2. The AlN epilayer with O-doped sputtered AlN NL has the highest optical transmittance.	
				3. The AlN epilayer with undoped sputtered AlN NL has the smoothest surface morphology and lowest TD density.	
AlN/MPSS	8–10	Sputtered AlN	S: 2.6×10^7	1. Misaligned AlN growth could be overcome by selecting an appropriate growth temperature.	[33]
			E: 1.8×10^9	2. Optimizing the PSS geometries is important for rapid coalescence of the AlN epilayer. In this paper, the grown AlN deviating from the *c*-axis on sapphire near *r*-plane sidewalls has less influence on the coalescence of AlN grown from the *c*-axis-oriented sapphire plane, compared to near *n*-plane sidewalls.	
AlN/NPSS	1	Sputtered AlN	TD: 6×10^8	1. The growth temperature can exert a strong impact on the crystalline quality of AlN epitaxial films by influencing the diffusion length of adatoms and lateral growth rate.	[34]
				2. The flat AlN films are realized on AlN/NPSS with a total coalescence at a growth temperature of 1300°C.	
AlN/FSS	85	–	–	1. Self-separation of AlN epitaxial film is achieved by the formation of voids at the AlN/sapphire interface during the HVPE growth at 1450°C.	[35]
				2. Voids are formed by decomposition of sapphire during the HVPE of the AlN epilayer, and their size is dominated by the heating time.	

[a]S, E, and TD represent screw, edge, and threading dislocation, respectively. EP means etching pit.

[b]PALE means pulsed atomic-layer epitaxy.

1250°C in Figs. 3(a)–3(c). The NL deposited at 950°C exhibited uniformly coalesced nucleation islands and the lowest surface roughness. By contrast, the NL deposited at 1050°C exhibited an uneven coalescence with rough surface morphology. The NL deposited at 1150°C in Fig. 3(c) exhibited very poor surface morphology with high undulations and insufficient covering on

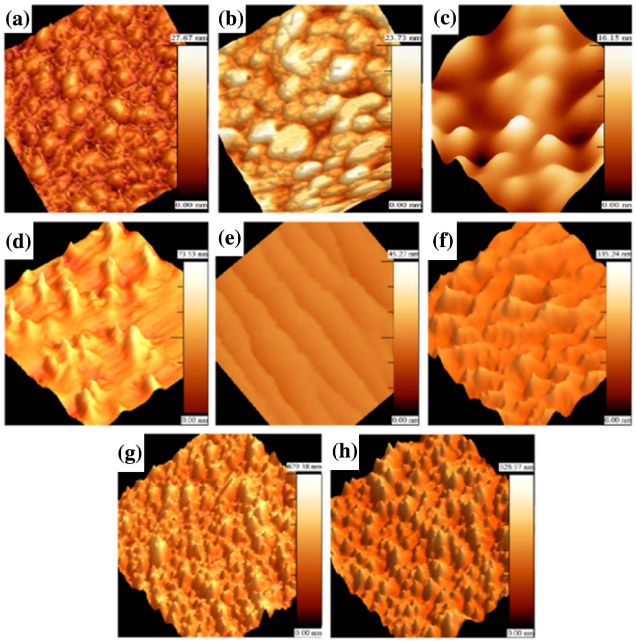

Fig. 3. AFM images of the NLs deposited at (a) 950°C, (b) 1050°C, and (c) 1150°C after being recrystallized at 1250°C. AFM images of AlN epitaxial films on NLs deposited at (d) 850°C, (e) 950°C, (f) 1050°C, (g) 1150°C, and (h) 1250°C. Reproduced with permission[65]. Copyright 2014, Elsevier.

the sapphire substrate. Then, they prepared five AlN epilayers grown on the NLs, which were deposited at 850°C, 950°C, 1050°C, 1150°C, and 1250°C in Figs. 3(d)–3(h). They found that a smooth surface with macro-steps and terrace features could have been achieved for the AlN epilayer grown on the NL deposited at 950°C. The average screw and edge dislocation densities of the AlN layer on the NL deposited at 950°C were estimated to be $9 \times 10^7\ cm^{-2}$ and $4.4 \times 10^9\ cm^{-2}$, respectively. Their research has demonstrated that the NL deposition temperature is an important growth parameter strongly related to producing evenly sized nucleation islands, thereby facilitating uniform coalescence of AlN epitaxial films.

2.5. p-doping of AlGaN

The p-doping of high-Al-content AlGaN alloys is still considered quite challenging after a few years of development. Achieving satisfactory p-doping AlGaN epilayers in the device level has turned out to be difficult. Many methods are developed to improve the low conductivity or poor contacts of p-AlGaN. For example, a standard solution is that a 10–50 nm p-AlGaN thin layer is generally grown on the top of the p-AlGaN cladding layer in UV LEDs; although the strong absorption of the thin p-AlGaN layer at the emission wavelengths is not avoided, it is still an effective way to realize a reasonably good contact, thereby ensuring stabilized hole injection efficiency into the active region of UV LEDs.

Generally, Mg, Zn, and Be can all be used for p-type doping. The corresponding activation energy (AE) of the Mg, Zn, and Be in GaN are 60, 160, and 370 meV[66]. The AE of the three doping elements increases with increasing Al content in the AlGaN layer. The AE of Be is the lowest among that of the three doping elements. However, Be atoms are so small that it possibly introduces interstitial atoms to compensate acceptors. Therefore, Mg generally acts as the impurity acceptor for p-doping of AlGaN alloys[67]. However, there are some negative factors that impede the development of p-type doping in high-Al-content AlGaN epilayers. They include the low solubility of acceptor dopants in AlGaN, the strong self-compensation effect resulting from the donor-like native defects, and the high AE of the Mg acceptor[68]. In recent years, many methods have been developed for increasing the solubility of Mg and reducing the AE of Mg in AlGaN p-doping of AlGaN, including delta doping, modulation doping, SL doping, co-doping, polarization-assisted doping, and multidimensional doping[69–76].

Chen *et al.* reported a type of indium-surfactant-assisted delta doping method for high hole concentration in Mg-doped p-$Al_{0.4}Ga_{0.6}N$ layers[71]. Compared with conventional delta doping, the indium-surfactant-assisted delta doping resulted in high hole concentration of $4.75 \times 10^{18}\ cm^{-3}$ and low sheet resistivity of $2.46 \times 10^4\ \Omega/sq$. These results originated from the enhanced Mg incorporation and reduced AE and compensation ratio by using indium surfactant. In addition, they also proposed that indium surfactant possibly triggers the stronger valence-band modulation, thereby further facilitating the decrease of AE and the increase of hole concentration. Sun *et al.* reported a kind of p-type polarization-doping method without using dopant in the AlGaN heterojunction phototransistor[77]. The strong polarization effect in AlGaN makes the p-type bulk doping possible with forming 3D hole gas induced by graded negative polarization[78]. The hole concentration stays around $1 \times 10^{17}\ cm^{-3}$ with the nearly linear change of Al composition with the depth. The concentration rapidly increases to $\sim 2 \times 10^{18}\ cm^{-3}$ near the AlGaN absorber/p-AlGaN interface with a steep decrease of Al composition. Zhang *et al.* reported an SL p-type electron blocking layer using in AlGaN DUV LED emitting at the peak wavelength of 270 nm[79]. The p-SL enables a high hole concentration in the EBL. As a result, the holes can be more easily injected into multiple quantum wells (MQWs). The increased holes injected into the MQW region can more efficiently recombine with electrons via radiative recombination, which can prominently reduce the electron-type leakage current. As a result, the external QE (EQE) of the DUV LED structure is increased by 100% and the nearly efficiency-droop-free DUV LED structure is obtained experimentally.

2.6. Methods for defect annihilation

The AlN epilayer grown on AlN/PSS is dominated by the ELOG[80]. There is growth mode transition from 3D to 2D during ELOG of the AlN epilayer grown on AlN/PSS, which can reduce the dislocations by bending, combining each other, and forming a closed loop. The V/III ratio strongly affects the surface mobility of Al adatoms that usually accompanies the transition of the growth mode between the longitudinal and transverse domination[81]. The low V/III ratio facilitates

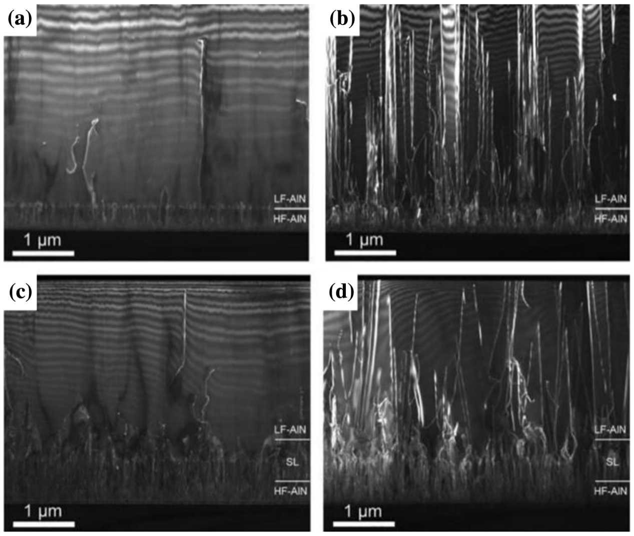

Fig. 4. Cross-section TEM images of AlN/FSS without AlN SL in the (a) $g = (0002)$ direction and (b) $g = (11\bar{2}0)$ direction. Cross-section TEM images of AlN/FSS without AlN SL in the (c) $g = (0002)$ direction and (d) $g = (11\bar{2}0)$ direction. Reproduced with permission[32]. Copyright 2021, American Institute of Physics Publishing.

the strong lateral growth and surface smoothing. The high V/III ratio accelerates the vertical growth rate, which produces abundant crystal boundaries to suppress the elongation of dislocation[82]. In addition, the dislocations can also be terminated on the internal surface of ELOG voids. Moreover, complete coalescence of AlN can induce high tensile stress owing to the mismatch of the thermal expansion coefficient between AlN and sapphire. The tensile stress will increase with the layer thickness increasing until it is strong enough to result in cracks on the AlN layer surface[31]. Inserting AlN SLs with alternating V/III ratios into AlN epitaxial films can reduce the dislocation density during the growth of epilayers[31,32,80,83,84]. That is because the dislocations are bent in the AlN SLs, as shown in Fig. 4[32]. The bent dislocations can provide an effective misfit dislocation segment to relax the stress, thus allowing wafers to survive from cracking during AlN growth. Furthermore, the bent dislocations can merge with each other to realize further defect annihilation. Wang *et al.* designed and fabricated four types of AlN epilayer structures with the above-discussed structure in Fig. 5(a)[82]. They found that sample C exhibited the lowest dislocation density of $7.4 \times 10^8\ \mathrm{cm^{-2}}$ among the four samples in Fig. 5(b). This result can be attributed to the introduction of AlN layers with high and low V/III ratios (H-V/III AlN and L-V/III AlN) and a three-period AlN SLs (LH-V/III AlN) structure. During the growth of H-V/III and L-V/III AlN layers, there was a transition of the growth mode from 3D to 2D. In this process, some dislocations were terminated by bending and merging with each other. It was noted that a large-batch annihilation of dislocations was achieved in LH-V/III AlN SLs. The majority of dislocations bent and merged, even forming close loops, so that few dislocations eventually propagated through the thick L-V/III AlN layer, as shown in Fig. 5(d).

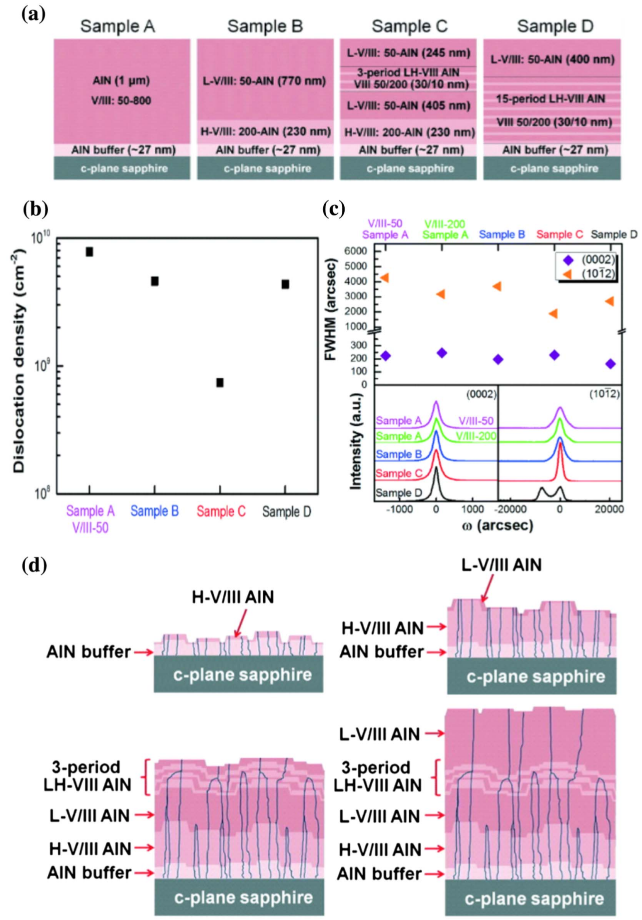

Fig. 5. (a) Illustration of samples with four types of distinct AlN layer structures. (b) Dislocation density of samples A–D. (c) FWHM and individual rocking curves of samples A–D. (d) Schematic illustration of the growth mechanism and dislocation annihilation for sample C. Reproduced with permission[82]. Copyright 2016, Elsevier.

We introduced voids into the AlN epilayers on FSS to realize similar defect annihilation in AlN/PSS, as shown in Fig. 6[85]. The AlN/NPSS templates were also fabricated for comparison. As shown in Fig. 6(b), most dislocations in AlN/NPSS templates were quickly annihilated on the nano-scaled mesa. However, the majority of dislocations in AlN/FSS remained propagating upward after the growth of high-temperature AlN-1 (HT-AlN-1) layers, as shown in Fig. 6(a). Although dislocations were reduced due to the introduction of the LT AlN layer, there was still a fairly high TDD in AlN/FSS in comparison to that in AlN/NPSS. It was noted that the large-batch annihilation of dislocations was realized in PALE-AlN layer with plenty of embedded voids. The majority of dislocations were wiped out on the void sidewalls, and only a small number of new dislocations were regenerated at the coalescence boundary of voids, as shown in Fig. 6(d). This function of the PALE voids embedded in AlN/FSS was quite similar with the voids spontaneously formed in the AlN/NPSS owing to ELOG of AlN, as shown in Fig. 6(b)[30]. In addition, the PALE-voids in AlN/FSS could offer channels to release the stress in the AlN epilayer grown on FSS, thereby

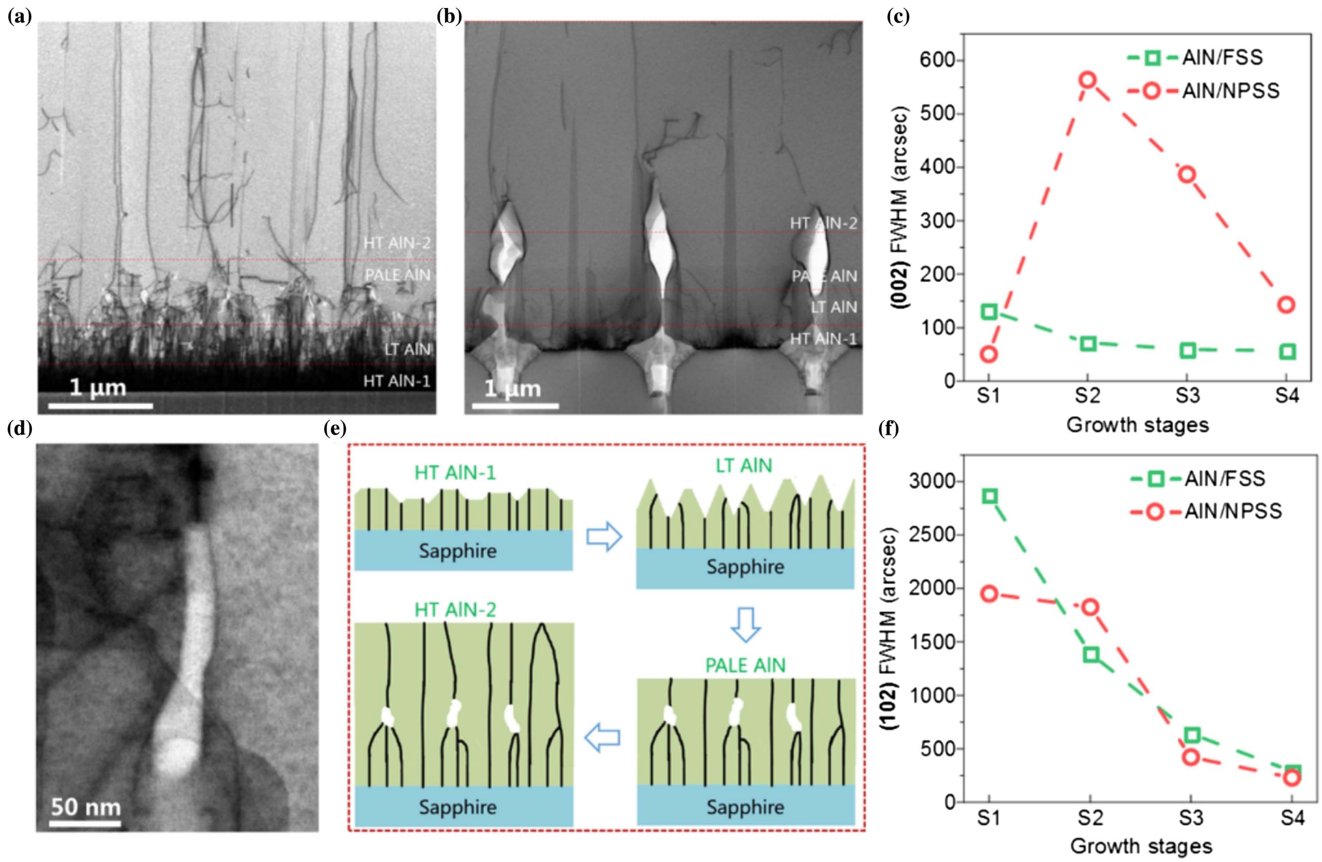

Fig. 6. Cross-section TEM images of (a) AlN/FSS and (b) AlN/NPSS in the $g = (11\bar{2}0)$ direction. FWHM for AlN/FSS and AlN/NPSS at different stages: (c) (002) reflection peak and (f) (102) reflection peak. (d) Enlarged TEM image of the void in AlN/FSS. (e) Schematic diagrams of dislocation behavior in AlN epitaxial film. Reproduced with permission[85]. Copyright 2020, Elsevier.

leading to tensile stress compared to that in AlN/NPSS. Beneficial from the above-mentioned merits, the AlN/FSS template with embedded voids exhibited a relatively low TDD of $1.7 \times 10^8\ \mathrm{cm}^{-2}$, as shown in Figs. 6(c) and 6(f).

3. Photovoltaic AlGaN Photodiode SBPDs

Numerous types of photovoltaic photodiodes, including Schottky barrier, MSM, p-n/p-i-n junction, and APDs, have been developed for SBPDs. In this section, we will review the current photovoltaic AlGaN photodiode SBPDs reported in recent years. Several reported photovoltaic AlGaN photodiode SBPDs are summarized in Table 2.

3.1. Parameters

The simplest configuration of an AlGaN photodiode SBPD includes an AlGaN absorption layer, metal electrodes, and external circuitry used to output electrical signals. The AlGaN absorption layer can be fabricated in various configurations, including wafers, thin films, or even nanostructures. Each of these configurations lends different properties to the fabricated photodetector that helps in enhancing one particular figure-of-merit or another. To characterize any device on the basis of its performance, one requires certain parameters[3]. For AlGaN SBPDs, the characteristics that judge its worth are mentioned below.

(1) Dark current (I_{dark})—It is the residual current that flows in the detector even in the absence of any incident light. It is measured in amperes.

(2) Responsivity (R)—It means the ratio of photogenerated current and incident optical power. The corresponding equation is shown in Eq. (1):

$$R = \frac{I_{\mathrm{light}} - I_{\mathrm{dark}}}{P_d A}, \tag{1}$$

where A, I_{light}, I_{dark}, and P_d are the effective illumination area, photocurrent, dark current, and incident optical power per unit area. It is measured in A/W.

(3) Response time (τ_R)—It indicates the time it takes for the detector output to change in response to changes in the input light intensity, which is called its response time. It is usually measured in two separate components — the rise time τ_r and the decay time τ_d. The τ_r is the time taken for the photodetector output level to change from 10% to 90% of the peak output level, while the decay time

Table 2. Summary of Performance Parameters on the Reported AlGaN SBPDs.

Absorption Layer	Device	I_{dark} (A)	R (mA/W)	Wavelength (nm)	D^* ($cm\,Hz^{1/2}\,W^{-1}$)	G	EQE	Ref.
$Al_{0.38}Ga_{0.62}N$	Schottky	4×10^{-12} @-20 V	90	274	2.6×10^{12}	–	42%	[86]
AlGaN/GaN	Schottky	$\sim1\times10^{-12}$ @-20 V	44	274	–	–	21%	[87]
$Al_{0.75}Ga_{0.25}N$	Schottky	$\sim1\times10^{-13}$ @-100 V	530	229	1.64×10^{12}	–	–	[88]
$Al_{0.4}Ga_{0.6}N$	Schottky	1.2×10^{-12} @-10 V	41	260	7.0×10^{14}	–	20%	[36]
AlGaN MQWs	p-n	1×10^{-13} @-0.5 V	100	250	–	–	50%	[89]
$Al_{0.4}Ga_{0.6}N$	p-i-n	$\sim1\times10^{-13}$ @-10 V	79	280	5.3×10^{13}	–	35%	[90]
$Al_{0.45}Ga_{0.55}N$	p-i-n	3×10^{-15} @-6 V	110	283	4.9×10^{14}	–	43%	[91]
$AlN/Al_{0.08}Ga_{0.92}N$	p-i-n	5.3×10^{-16} @ $\sim$ 0 V	62	247	4.5×10^{13}	–	30%	[92]
$Al_{0.45}Ga_{0.55}N$	p-i-n	5×10^{-6} @-5 V	136	282	–	–	72%	[93]
$Al_{0.4}Ga_{0.6}N$	p-i-n	5×10^{-15} @-10 V	93	280	7.5×10^{14}	–	42%	[94]
$Al_{0.4}Ga_{0.6}N$	p-i-n	1.6×10^{-12} @-10 V	211	289	6.1×10^{14}	–	92%	[95]
$Al_{0.4}Ga_{0.6}N$	MSM	10^{-15} @20 V	140	272	–	–	64%	[96]
$Al_{0.42}Ga_{0.58}N$	MSM	2×10^{-12} @20 V	–	285	–	–	–	[97]
$Al_{0.6}Ga_{0.4}N$	MSM	$\sim10^{-15}$ @ $\sim$ 0 V	2750	250	–	–	–	[98]
AlGaN/Al NPs	MSM	$\sim10^{-13}$ @0 V	288	288	–	–	–	[99]
$Al_{0.4}Ga_{0.6}N$	APD	3.3×10^{-12} @-10 V	79.8	270	–	> 2500 @-65 V	37%	[100]
$Al_{0.38}Ga_{0.62}N$	APD	3×10^{-13} @-20 V	132	281	–	3000 @-91 V	58.2%	[101]
$Al_{0.4}Ga_{0.6}N$	APD	10^{-12} @-100 V	98	262	–	4000 @-177 V	46%	[102]
$Al_{0.4}Ga_{0.6}N$	APD	1.5×10^{-10} @-60 V	150	280	–	12,000 @-84 V	50%	[103]
$Al_{0.2}Ga_{0.8}N/Al_{0.45}Ga_{0.55}N$	APD	$\sim10^{-11}$ @-20 V	–	275	–	55,000 @-109 V	98.5%	[104]
AlGaN/GaN	APD	5×10^{-10} @-86 V	–	275	–	10,000 @-92 V	–	[105]

is the time taken for the output level to change from 90% to 10% of the peak output level. It is measured in seconds.

(4) Detectivity (D^*)—It characterizes how well a weak signal can be detected compared to the detector noise. D^* is expressed by Eq. (2):

$$D^* = R\sqrt{\frac{A}{2Q_e I_{dark}}}, \quad (2)$$

where A, I_{dark}, Q_e, and R are the effective area of illumination, dark current, electronic charge, and responsivity, respectively. It is measured in $cm\,Hz^{1/2}\,W^{-1}$ (Jones).

(5) Quantum efficiency (QE)—It indicates the ability of the photodetector to convert the input optical signal to the output electrical signal. The two sub-components are the internal QE (IQE) and EQE. IQE is defined as ratio of the number of electron–hole pairs generated in the semiconductor to the number of incident photons per second, whereas EQE represents the ratio of the number of electron–hole pairs collected (contributing to the photocurrent) to the number of incident photons per second. Both IQE and EQE are measured in terms of percentages. Usually, EQE is the preferred figure-of-merit in AlGaN SBPDs and is determined by Eq. (3):

$$\text{EQE} = \frac{Rhc}{Q_e \lambda}, \quad (3)$$

where R, h, c, Q_e, and λ are the responsivity, Planck's constant, velocity of light, electronic charge, and the wavelength of the incident light, respectively.

(6) NEP—It indicates the minimum optical input power to achieve a signal-to-noise ratio of unity in a 1 Hz output bandwidth.
(7) Gain (G)—It characterizes the number of photogenerated carriers accumulated via the electrodes divided by the absorbed photons. The corresponding equation is exhibited in Eq. (4):

$$G = \log_{10}\left(\frac{P_{\mathrm{out}}}{P_{\mathrm{in}}}\right), \tag{4}$$

where P_{out} is the power of output electrical signals, and P_{in} is the power of input optical signals.

3.2. Schottky barrier photodiodes

A typical Schottky barrier SBPD is made up of a metal contact layer and a semiconductor absorption layer. The metal/semiconductor junction exhibits rectifying behavior originated from the electrostatic barrier induced by different work functions of the metal and semiconductor. This electrostatic barrier is also called the Schottky barrier. The SBPDs based on Schottky barrier photodiodes exhibit many advantages, including low dark current, short response time, high QE, high responsivity, and possible zero-bias operations. Nevertheless, the incident light needs to penetrate the metal electrode to interact with the semiconductor so that the metal electrode layer needs to be fabricated into a very thin semitransparent layer, whose absorption coefficient is too high to limit further application of the Schottky barrier photodiodes structure in SBPDs.

Biyikli *et al.* reported a type of $Al_{0.38}Ga_{0.62}N/GaN$ solar-blind Schottky photodiode with low noise and high detectivity[86]. The SBPD exhibited a fairly low dark current density of 1.8 nA/cm^2 and a maximum EQE of 42% at 267 nm. The photovoltaic detectivity of the SBPD was more than $2.6 \times 10^{12}\ \mathrm{cm\,Hz^{1/2}\,W^{-1}}$. Cheng *et al.* investigated the temperature dependence of I-V characteristics of AlGaN-based Schottky SBPDs[106]. The ideality factor decreased from 2.57 to 1.75, while the barrier height increased from 0.75 to 1.14 eV in the temperature range of 198–323 K. The I-V characteristics at a small forward current were intersectant at 273, 298, and 323 K and almost parallel at 198, 223, and 248 K. This crossing of the I-V characteristics was an inherent property of Schottky diodes, and the almost parallel curves could be well explained by thermionic field emission theory.

3.3. MSM

AlGaN MSM photodetectors basically consist of a lightly-doped/undoped AlGaN absorption layer and two metal electrodes deposited on the AlGaN surface to form back-to-back Schottky barrier junctions[15,107–109]. In general, the metal electrodes are fabricated into interdigitated shapes. This electrode can effectively shorten the migration distance of photogenerated carriers and simultaneously stabilize the photosensitive surface area. However, due to the presence of Schottky barriers, separation and migration of photogenerated electron–hole pairs need a relatively high bias. In addition, AlGaN MSM SBPDs normally exhibit relatively lower dark current in comparison to photoconductors because of the rectifying feature of Schottky contacts. Moreover, AlGaN MSM SBPDs also possess fast response speed resulting from the carrier transit time owing to intrinsically low capacitance per unit area. High photoconductive gain is also possible in MSM SBPDs. Although MSM SBPDs usually exhibit relatively low EQE owing to the electrode shadowing effect, it can be relieved by optimizing the electrode geometry and using semitransparent electrodes[110–112]. In a word, with good device performance, simple device configuration, and low fabricating cost, MSM SBPDs are extremely attractive for monolithic integration with other components on optoelectronic circuits.

In general, MSM SBPD structures include two metal electrodes with back-to-back Schottky contact. The ideal MSM SBPDs with Schottky contact are not expected to exhibit a photoconductive gain, and the responsivity should not change with the applied bias. However, most of the present AlGaN-based MSM SBPDs exhibit high photoconductive gain and responsivity[108,113]. The reverse leakage is believed to result from the trapping of dislocations and defects in the active region or around the metal-semiconductor interface, which leads to persistent photoconductive effects and high photoconductive gain[114]. For high-Al-content AlGaN SBPDs, there are amounts of threading and screw dislocations generated during the actual heteroepitaxial growth process. If high-density threading and screw dislocations exist in the conductive path, a high reverse leakage current will be generated in the Schottky contact[115,116]. In order to improve the performance of AlGaN-based MSM SBPDs, it is essential to explore the carrier transport and photoconductive gain mechanisms. For example, Zhang *et al.* fabricated the MSM-type $Al_{0.55}Ga_{0.45}N$ SBPD and explored the photoconductive gain mechanisms of the device[117]. The device exhibited high responsivity and EQE because of the photoconductive gain effect. The current exhibited strong temperature dependence in the range of 4–10 V. Moreover, the authors used the Poole–Frenkel emission model and changed the space charge regions to explain the carrier transport and photoconductive gain mechanisms of the AlGaN SBPD, respectively.

In 2012, Xie *et al.* reported a kind of $Al_{0.4}Ga_{0.6}N$ MSM SBPD with ultralow dark current for HT photodetection[96]. The MSM SBPD exhibited a fA-scaled ultra-low dark current at room temperature both under 20 V bias and 300 V breakdown voltage. The maximum room-temperature QE of the SBPD was 64% at a radiation wavelength of 275 nm under 10 V bias. The room-temperature soalr-blind/ultraviolet (SB/UV) rejection ratio was up to 10^4. Even at 150°C, the dark current of the AlGaN MSM SBPD still was stabilized in the femto-ampere (fA) range with a reasonable SB/UV rejection ratio of more than 8000. The outstanding results were attributed to the application of the HT-AlN template. That was because HT could relax tensile stress and rearrange the AlN lattice to realize low defect density in the AlN template, thereby facilitating the growth of high-quality AlGaN epitaxial film.

Averine *et al.* fabricated a kind of $Al_{0.3}Ga_{0.7}N/GaN$ MSM SBPD via using metal-organic chemical vapor deposition

(MOCVD)[15]. They investigated the effects of different buffer layers on the performance of MSM SBPDs. The SBPD on GaN buffer layer exhibited the higher response speed than those on the AlN buffer layer. However, the SBPD on the AlN buffer layer exhibited a smaller dark current and a larger UV/visible rejection than that on the GaN buffer layer. Researchers further studied the interesting experimental results. They found that carrier transit time and resistance-capacitance time (RC-time) constants are able to exert a strong influence on the response speed of the SPBDs at low optical excitation levels. Nevertheless, under high illumination intensity, the accumulation of charge and screening of the dark electric field would modify the drift conditions of the photogenerated carriers, thereby leading to serious distortion of response and reduced efficiency.

Brendel *et al*. investigated the influence of absorption layer thickness on the photodetection performance of top and bottom-illuminated $Al_{0.5}Ga_{0.5}N$ SBPDs[118]. The AlGaN SBPD exhibits an EQE of up to 67% at 50 V under bottom illumination when the $Al_{0.5}Ga_{0.5}N$ layer was 0.5 μm thick. When the absorber layer was 0.1 μm thick, the EQE of the SBPD also reached 50%. The experimental results were well in accordance with 2D drift-diffusion modeling, which indicates there was an extraction of photoexcited holes confined along the AlGaN/AlN interface because of a polarization-induced space charge region.

Recently, photonic crystals have been widely applied in fabricating SBPDs. Photonic crystals can be applied for reflective modulation of light by generating photonic bandgaps. When the electromagnetic wave propagates in the optical structure with periodic refractive index variation, the photonic bandgap will be formed to suppress the light propagation in corresponding bands due to the existence of Bragg scattering[38,119,120]. Based on characteristics of photonic crystals, Tan *et al*. designed a type of back-illuminated MSM SBPD integrated with SiO_2/Si_3N_4 photonic crystal layers, as shown in Fig. 7(a)[97]. The $Al_{0.52}Ga_{0.48}N/Al_{0.55}Ga_{0.45}N$-based SBPD exhibited manifest solar-blind photodetection capability with a distinct responsivity peak at a wavelength of 285 nm and an ultralow dark current of 2 pA at 20 V bias, as shown in Fig. 7(d). The light/dark current ratio was up to 4000. Furthermore, the MSM SBPD obtained a noteworthy narrowband detection property, which could result from the impurity and defect levels in the heterostructure and optical modulation by photonic crystal layers.

3.4. p-n and p-i-n

AlGaN p-n junction photodiodes are typical photovoltaic photodiodes that are geometrically made up of a piece of p-AlGaN and a piece of n-AlGaN. Therefore, when operating at zero bias,

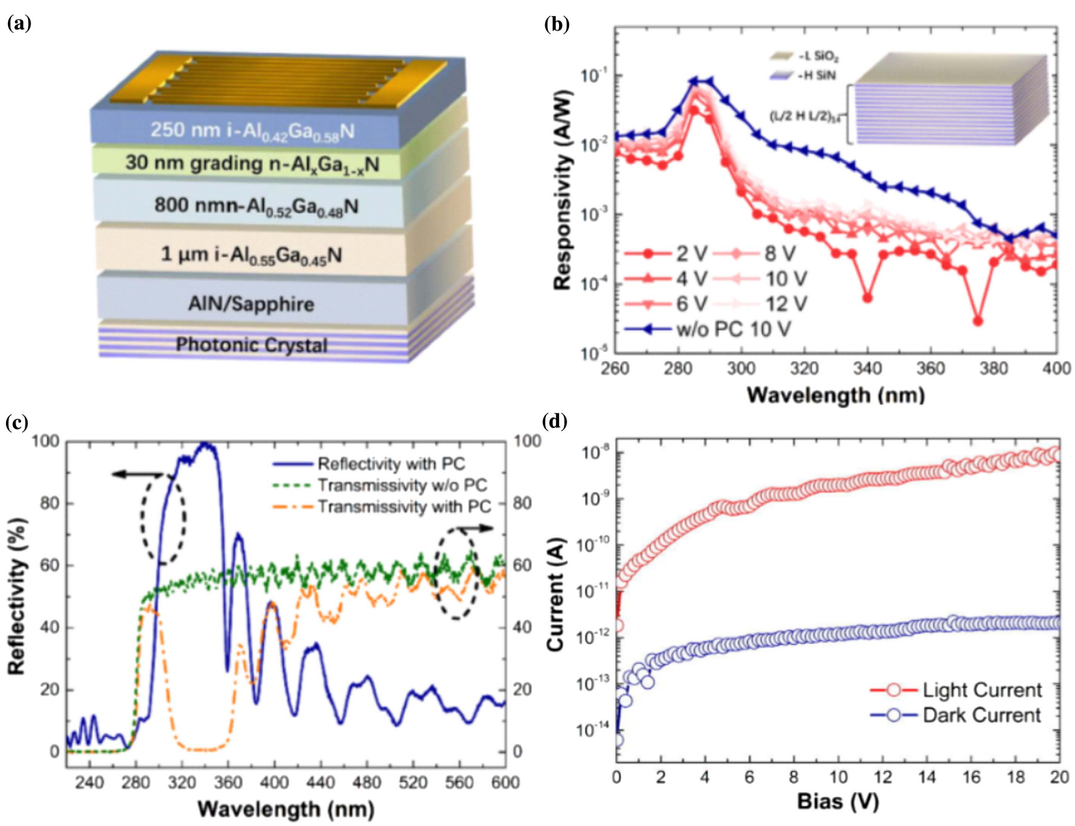

Fig. 7. (a) Schematic diagram of AlGaN-heterostructure MSM SBPD. (b) Responsivity of the MSM SBPD with and without photonic crystals. (c) Reflectivity and transmissivity of the AlGaN MSM SBPD with and without photonic crystals. (d) *I-V* characteristics of AlGaN MSM SBPD. Reproduced with permission[97]. Copyright 2021, American Institute of Physics Publishing.

the depletion region is spontaneously formed at the interface of two semiconductors, and a built-in electric field is concomitantly created. Consequently, an energy barrier is formed near the interface to prevent charge carriers freely transferring across the junction because of the discontinuity in allowed energy states of the two semiconductors at an equilibrium state. Therefore, p-n photodiodes normally exhibit rectifying behavior, which indicates an asymmetric *I-V* characteristic in the darkness. When the AlGaN p-n photodetectors are placed in the solar-blind illumination, the photons whose energy is higher than the bandgap of AlGaN are absorbed by the AlGaN layer, thereby creating the photogenerated electron–hole pairs on both sides of the junction. Due to the built-in electric field in the depletion region, only the minority carriers on both sides of the junctions can traverse across the depletion region. AlGaN p-n SBPDs have many advantages, including a low working bias, high input impedance, high working frequency, and integration capability that is useful for manufacturing technologies and semiconductor planar processes[1,89,121,122].

Muhtadi *et al.* reported a type of high-speed solar-blind AlGaN p-n junction photodetector integrated with high-Al-content AlGaN MQWs, as shown in Fig. 8(a)[89]. The MQWs were composed of four pairs of $Al_{0.64}Ga_{0.36}N/Al_{0.34}Ga_{0.66}N$. The fabricated device exhibited a prominent responsivity of up to 0.1 A/W at a 250 nm radiation wavelength with >50% EQE, as shown in Fig. 8(c). The high responsivity was deemed to attribute to high-Al-content MQWs. In addition, the dark current was less than 0.1 pA at 0.5 V reverse bias, as shown in Fig. 8(b). The readout RC-limited time response was measured as 0.4 μs, and an achievable detector RC-limited time response of 2 ns was estimated. However, the device did not exhibit internal gain, which was supposed to result from high response speed.

Unlike the p-n junctions, the width of the depletion region in the p-i-n junctions is primarily determined by the thickness of the intrinsic layer. Although concurrently increasing the transit time of photogenerated carriers and reducing the response speed of the photodetectors, a thick intrinsic layer can ensure sufficient light absorption, thereby improving the EQE of the photodetectors. That will facilitate reducing the junction capacitance and the RC-time constant. Hence, it is necessary to compromise the design according to demands of real applications[123].

In 1999, Parish *et al.* reported a AlGaN-based p-i-n SBPD with a cut-off wavelength of 285 nm. The measured dark current density was as low as 10 nA/cm^2 at 25 V bias. The peak responsivity was up to 50 mA/W. In addition, the SBPDs exhibited relatively short response time as low as 4.5 ns for 90%-to-10% fall time. Subsequently, Kuryatkov *et al.*[92] brought up with a novel type of solar-blind p-i-n photodetector with 247 nm cut-off wavelength. The absorption layers of the p-i-n SBPDs were made up of period $AlN/Al_{0.08}Ga_{0.92}N$ SLs. It was worth noting that the fabricated SBPD possesses a relatively low dark current density of 3 pA/cm^2 and a high resistance of 6×10^{14} Ω at zero bias. The 10 V responsivity was up to 62 mA/W.

Then, Tut *et al.* reported a type of AlGaN p-i-n SBPDs with high breakdown voltage and detectivity via using MOCVD[94].

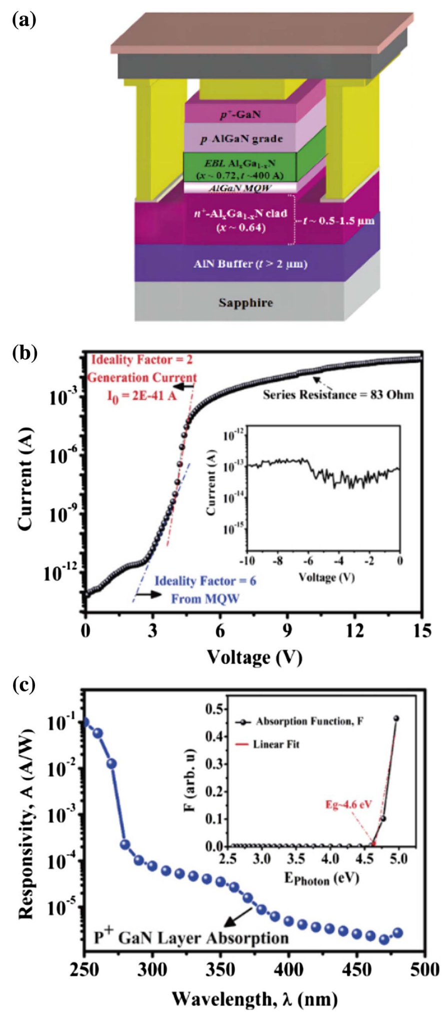

Fig. 8. (a) Device structure of the AlGaN MQWs SBPD. (b) *I-V* characteristic of $Al_{0.64}Ga_{0.36}N/Al_{0.34}Ga_{0.66}N$ SBPD in the dark. (c) Responsivity spectrum of AlGaN MQWs SBPD at -0.5 V. Reproduced with permission[89]. Copyright 2017, Institute of Physics.

The dark current was measured to be only ~5 fA at 10 V bias. Moreover, the breakdown voltage was higher than 200 V. The responsivities of the SBPD were 52 and 93 mA/W at 280 nm as well as 0 and 40 V reverse biases, respectively. The corresponding EQEs at 0 and 40 V reverse biases were 42% and 22%, respectively. The solar-blind spectrum detectivity of the fabricated device was up to 7.5×10^{14} cm Hz$^{1/2}$ W^{-1} at 280 nm.

Researchers at the Fraunhofer Institute reported AlGaN-based p-i-n SBPDs with different active regions[124]. They regulated the bandgap of $Al_xGa_{1-x}N$ by changing the Al content and integrating it with an optical filter to obtain the solar-blind response. They subsequently packaged the $Al_xGa_{1-x}N$ SBPDs in TO-18 headers. The packaged SBPDs exhibited a prominent responsivity of 0.11 A/W with 57% EQE. The room-temperature dark current density was measured as 30 pA/cm^2 at 3 V reverse bias, yielding a detectivity of more than 4×10^{14} cm Hz$^{1/2}$ W^{-1}.

Inserting MQWs into the depletion region of p-i-n SBPDs can also facilitate improvement of performance[125,126]. Inserted

MQWs can generate current gain due to their strong hole confinement effect and the quantum confinement Stark effect (QCSE). That will induce long carrier lifetime and unipolar carrier transport, which are the key factors for photoconductive gain. Guo *et al.* brought up a type of AlGaN p-i-n SBPDs with MQWs insertion layers[126]. At zero bias, this novel device structure exhibited a relatively high peak responsivity of 0.425 A/W at a radiation wavelength of 233 nm. The corresponding EQE was up to 226%, which confirmed the existence of internal current gain. Compared with the device structure without MQWs, the gain of AlGaN p-i-n SBPD with MQWs was estimated to be about 10^3 in magnitude in comparison to that of the p-i-n SBPD without MQWs. Moreover, the large-band offset in the MQWs could suppress the dark current to achieve a better signal-to-noise ratio (SNR). Their investigation is very important in the fabrication of high-gain SBPDs with vertical structure at low or even zero bias.

3.5. Avalanche photodiodes

The APD is a type of photodiode that uses the avalanche production of carriers at a high reverse bias[101]. The APD exhibits two modes: linear and Geiger. When avalanche breakdown occurs and the device achieves a large multiplication gain, the device works in the Geiger mode, which plays a significant role in the field of single-photon detection. The multiplication factor can be expressed by the following equation:

$$M = \frac{1}{1 - \int_0^L \alpha(x)\mathrm{d}x}, \tag{5}$$

where L is the carrier movement length, and α is the multiplication coefficient of carriers. The impact ionization coefficient is related to the natural characteristic and external impactors such as electric field intensity and operation temperature. The multiplication gain G_M can be calculated by

$$\mathrm{GM} = \frac{I_{M,\mathrm{light}} - I_{M,\mathrm{dark}}}{I_{0,\mathrm{light}} - I_{0,\mathrm{dark}}}, \tag{6}$$

where I_M and I_0 are the multiplied and unmultiplied currents, respectively.

The reported APDs involve the various structures discussed above, including Schottky barrier, p-n, and p-i-n structures[127]. In particular, a separate absorption and multiplication (SAM) structure has also been proposed to enhance APD SBPD performance[128–130]. During solar-blind UV irradiation, the photogenerated electrons and holes in the SAM structure are separated and pulled to p-AlGaN and n-AlGaN regions by the electric field, respectively. The carriers are accelerated in the multiplication region, thereby causing massive impact ionization and triggering avalanche events. When reaching their respective electrode regions, these photogenerated electrons and holes still retain high velocity and create exponentially additional electron–hole pairs from the lattice via impact ionization. This characteristic can make APDs qualified in the detection of weak UV signals. Considering the materials used in APD SBPDs, high-Al-content AlGaN APD SBPDs grown on AlN/sapphire are more qualified than those grown on GaN templates.

In 2005, McClintock *et al.* observed avalanche multiplication in AlGaN p-i-n SBPDs[131]. Upon solar-blind UV illumination, the optical gain showed a soft breakdown starting at relatively low electric fields, eventually saturating without showing a Geiger mode breakdown. The devices achieved maximum optical gain of 700 at a reverse bias of 60 V.

Then, Sun *et al.* reported a type of AlGaN APD SBPD with high multiplication gain[100]. The fabricated APD SBPD exhibited a zero-bias responsivity of 79.8 mA/W at 270 nm with 37% EQE. Multiplication gain was up to 2500 at 62 V reverse bias, which was a relatively high value among the reported AlGaN APD SBPDs. Shao *et al.* reported a high-performance AlGaN SAM-APD SBPD on the AlN template via using MOCVD[103]. It was worth noting that they applied a photoelectrochemical treatment process after mesa etching to reduce damage originating from the etching process when preparing the device. The device exhibited a relatively low leakage current and a record-high gain of 1.2×10^4 at 84 V reverse bias.

The AlGaN heterostructure is receiving increasing attention for its excellent properties on APD SBPDs[39,105,132]. Shao *et al.*[104] reported a type of AlGaN-heterostructure APD SBPD with the multiplication region composed of high/low-Al-content AlGaN layers. The APD SBPD exhibited an ultrahigh gain of 5.5×10^4 at 109 V reverse bias owing to improvement of the average hole ionization coefficient resulting from the AlGaN heterostructure. In addition, the large potential barrier to the conduction band was generated at the interface of the $Al_{0.2}Ga_{0.8}N/Al_{0.45}Ga_{0.55}N$ heterostructure. The potential barrier could impede the transport of electrons by weakening the electron-initiated multiplication, thereby suppressing the noise of the APD SBPDs. The simulated result also confirmed this effect in the heterostructure.

Employing distributed Bragg reflectors (DBRs) can also improve the gain of AlGaN APD SBPDs[133–136]. Yao *et al.* designed AlGaN-based SAM-APD SBPDs with a dual-periodic DBR that was composed of 13 pairs of $AlN/Al_{0.55}Ga_{0.45}N$ (A/B) and 12 pairs of $Al_{0.64}Ga_{0.36}N/Al_{0.77}In_{0.23}N$ (C/D) via using the software Atlas (Silvaco), as shown in Fig. 9[133]. The DBR exhibited a high reflectivity of $> 90\%$ and a wide stop band of 40 nm within the solar-blind irradiation, as shown in Fig. 9(c). In addition, an SAM structure of $Al_{0.15}Ga_{0.85}N/Al_{0.15}Ga_{0.85}N$ with an n-graded AlGaN charge layer was used to improve the avalanche gain and breakdown voltage. This SAM structure allowed the injection of nearly pure holes into the multiplication region and benefited from a high ionization coefficient for holes. The SAM-APD SBPDs with a dual-periodic DBR exhibited a cut-off wavelength of 290 nm. The peak responsivity reached 0.184 A/W at 284 nm, as shown in Fig. 9(d). It was noted that the gain of SAM-APD SBPDs with dual-periodic DBR was up to 4.59×10^6 at 65.4 V. Chang *et al.* designed a kind of DBR with a tri-layer period structure for solar-blind UV light, as shown in Fig. 9(e)[134]. The DBR was composed of 20 pairs of AlGaN

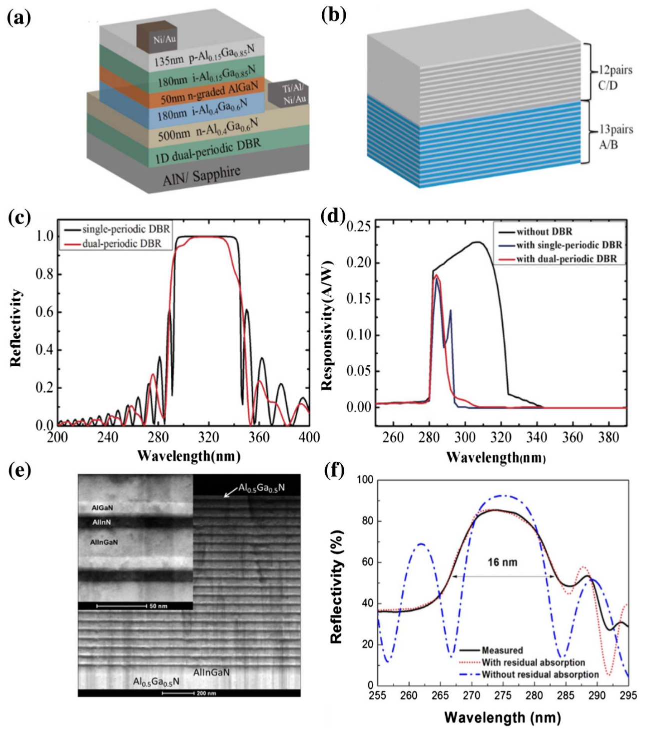

Fig. 9. Schematic diagrams of (a) $Al_{0.15}Ga_{0.85}N/Al_{0.15}Ga_{0.85}N$ SAM-APD SBPD and (b) dual-periodic DBR. (c) Reflectivity of single- and dual-periodic DBR. (d) Responsivity of the SAM-APD SBPDs with single-/dual-periodic and without DBR at 10 V reverse bias. The single-periodic DBR is composed of 25 pairs of $AlN/Al_{0.55}Ga_{0.45}N$ (A/B). Reproduced with permission[133]. Copyright 2017, Institute of Physics. (e) Cross-section TEM image of the DBR with 20-pair AlGaN/AlInN/AlInGaN layers. (f) Measured and simulated reflectivity of the DBR with 20-pair AlGaN/AlInN/AlInGaN layers. Reproduced with permission[134]. Copyright 2016, Springer Nature Publishing Group.

(16 nm)/AlInN (12 nm)/AlInGaN (28 nm). Composition-graded AlInGaN interlayers were used as transition layers to relieve the lattice mismatch between AlInN and AlGaN. Therefore, atomic-level-flatness interfaces were realized in the DBR grown on the AlGaN template. The state-of-the-art DBR structure exhibited a peak reflectivity of 86% at the center wavelength of 274 nm and a stop band with a full width at half-maximum of 16 nm, as shown in Fig. 9(f). The measured peak reflectivity of the DBR was lower than the theoretically calculated value because of the residual absorption from the AlGaN layer. The merit of this tri-layer structure could be used to control the strain of multi-period DBRs for more efficient solar-blind UV photodetection.

3.6. Phototransistor

Another important device structure for photodetection is phototransistors due to the possibility of controlling the channel current by gate bias. By changing the gate bias (V_{GS}), the dark current of the phototransistor can be controlled, and hence the detectivity and photo-to-dark-current ratio can be improved by using this device structure[137–139].

In 2018, Armstrong *et al.* observed solar-blind photodetection induced by defects in $Al_{0.85}Ga_{0.15}N/Al_{0.70}Ga_{0.30}N$ high electron mobility transistors (HEMTs)[140]. The fabricated HEMT SBPD exhibited a rather high peak responsivity of 4.9×10^4 A/W in the saturation mode. They attributed this achievement to the sub-bandgap absorption by defect states. Understanding the intrinsic physical mechanism will conceive the high photosensitivity in AlGaN-based phototransistors. The photogenerated holes can be captured by the defect states in AlGaN metal-semiconductor field-effect transistors (MESFETs), thereby leading to an increase in the steady-state electron density in the channel[141]. This phenomenon arises from optical gain. For AlGaN HEMTs, optical gain is attributed to generation of free holes in the barrier layer, thereby enhancing the 2D electron gas (2DEG) or collection of free carriers generated in the channel layer by the depletion region under the gate[142]. In addition, sub-bandgap absorption by either the barrier or the channel layer has also been observed to produce strong thresholds in photoresponse in AlGaN HEMTs, indicating that deep level defects can function in the photoresponse[143]. In this study, the defect-mediated solar-blind UV photoresponsivity in $Al_{0.85}Ga_{0.15}N/Al_{0.70}Ga_{0.30}N$ HEMT causes slow photocurrent rise and fall times, but electrical pulsing is used to improve the bandwidth at the cost of optical gain. As a result, operating $Al_{0.85}Ga_{0.15}N/Al_{0.70}Ga_{0.30}N$ HEMTs in this dynamic mode achieved a 25 Hz bandwidth with a peak responsivity of 2.9×10^5 A/W in accumulation and 5.1×10^3 A/W in pinch-off mode. In addition, the authors also reported a kind of visible-blind $Al_{0.45}Ga_{0.55}N/Al_{0.30}Ga_{0.70}N$ HEMT in this paper.

Zhang *et al.* reported a high-performance UV phototransistor (UVPT) based on the AlGaN/GaN HEMT with a record high peak responsivity[144]. When the AlGaN/GaN UVPT is bias at the off state, a very low dark current of 20 pA can be achieved. In addition, a record solar-blind photoresponsivity is achieved up to 3.6×10^7 A/W at 12 $\mu W/cm^2$ under 265 nm illumination when the device is biased at the off state. In addition, the authors investigated the V_{GS}-dependent photoresponse of AlGaN/GaN HEMT under 265 nm and 365 nm illumination. They found that a negative V_{GS} can prominently enhance the electric field of the AlGaN barrier, thereby significantly shortening the rise/decay time of AlGaN/GaN HEMT for 265 nm solar-blind photodetection, especially under weak light conditions. In contrast, V_{GS} has negligible influence on the rise/decay time for 365 nm UV illumination. That is because the GaN channel has a deep absorption depth, and the device mainly works in the photoconductive mode. Their work paves the way for the development of next generation SBPD.

Subsequently, Yang *et al.* investigated the temperature dependence of UV photodetection behavior in AlGaN/GaN UVPT under 265 nm illumination[145]. The authors found that the photocurrent of a device changes in a parabolic mode with the temperature continuously increasing from room temperature to 250°C. This results from the competing process between the generation and recombination of photogenerated electron–hole pairs in the AlGaN/GaN UVPT at room and high temperature. The optimal operating temperature for the fabricated AlGaN/GaN UVPT is 50°C. The corresponding peak responsivity is up to 1.52×10^5 A/W under a light intensity of 45 μW/cm^2. In addition, the photoresponse time of the device also exhibited prominent temperature dependence. The device shows the shortest rise time of 50 ms at 100°C, while the decay time is monotonically reduced with the temperature increasing to 250°C. In a word, their work highlights the promising future of such device configurations for harsh environment applications.

4. Enhanced Techniques of AlGaN SBPDs

In previous sections, we introduced the research achievements of AlGaN epitaxial films, AlN/sapphire templates, and various kinds of photovoltaic AlGaN-based SBPDs with various configurations. In this part, we will review the recent enhanced techniques of AlGaN SBPDs. Several reported enhanced techniques for photovoltaic AlGaN photodiode SBPDs are summarized in Table 3.

4.1. Polarization effect

AlGaN alloys possess strong spontaneous and piezoelectric polarization. The ionic bond component and the non-centro-symmetrical crystal structures result in spontaneous polarization. In addition, the tensile or compressive strain can alter the bond angle and further result in piezoelectric polarization. During the formation of AlGaN heterostructures, a steady layer filled with high-concentration electrons, which is also called 2DEG, is generated at the interface of heterostructures owing to the abovementioned polarization effect. The polarization effect has significant impacts on the performance of III-nitrides-based devices. For example, the success in photodetectors, which are based on HEMT, strongly depends on the 2DEG resulting from the polarization effect. For AlGaN SBPDs, if the built-in field in the absorption layer can be enhanced by controlling the polarization, the photogenerated electron–hole pairs can be separated more efficiently, and thus the carrier collection efficiency can be improved.

Chen *et al.* reported a kind of polarization-graded AlGaN SBPD grown on pre-grown AlN templates via using low-pressure MOCVD (LP-MOCVD), as shown in Fig. 10[149]. The growth rate modulation method is adopted to further improve the quality of the AlN template based on the method of introducing a mesothermal AlN (MT-AlN) interlayer, while an n-$Al_xGa_{1-x}N$ gradient layer is introduced in the AlGaN-based p-i-n SBPD to build a polarization-induced field. As a result, the SBPD exhibited a low dark current density of $\sim10^{-11}$ A/cm^2 and a high spectral responsivity of 0.204 A/W with an EQE of up to 95%, as shown in Figs. 10(b)–10(d). That is because the polarization-graded n-$Al_xGa_{1-x}N$ epilayer can prominently reduce the loss of the photon-generated carriers owing to the reflection or trapping effect at the interface of the heterojunction, which

Table 3. Summary of Performance Parameters on the Enhanced Techniques of Reported AlGaN SBPDs.

Absorption Layer	Enhanced Technique	I_{dark} (A)	R (A/W)	Wavelength (nm)	Ref.
$Al_{0.6}Ga_{0.4}N/Al_{0.5}Ga_{0.5}N$	Polarization	10^{-11} @5 V	10^6	280	[146]
$Al_{0.6}Ga_{0.4}N/Al_{0.45}Ga_{0.55}N$	Polarization	$\sim3\times10^{-12}$ @-2 V	3.1	280	[147]
$Al_{0.1}Ga_{0.9}N/GaN$	Polarization	$\sim1\times10^{-13}$ @0 V	12.5	266	[148]
$Al_xGa_{1-x}N$	Polarization	$\sim10^{-11}$ @0 V	0.204	274	[149]
AlN	Surface modification	$\sim10^{-12}$ @-2 V	6×10^{-4}	200	[150]
$Al_{0.6}Ga_{0.4}N$	Surface modification	$\sim10^{-14}$ @ ~ -2.5 V	7.6	250	[151]
$Al_{0.6}Ga_{0.4}N$	Surface modification	$\sim10^{-15}$ @0 V	2.75	250	[98]
$Al_{0.5}Ga_{0.5}N/Al_{0.4}Ga_{0.6}N$	Surface modification	1.47×10^{-11} @ $\sim$ 5 V	∼100	260	[152]
AlGaN	LSPR	$\sim10^{-13}$ @0 V	0.288	288	[99]
$Al_{0.54}Ga_{0.46}N$	LSPR	$\sim10^{-13}$ @0 V	2.34	269	[153]
$Al_{0.4}Ga_{0.6}N$	LSPR	$\sim2\times10^{-13}$ @20 V	0.3	265	[154]
$Al_{0.4}Ga_{0.6}N$	LSPR	10^{-14} @ $\sim$ 0 V	2.7	280	[155]
Ru/AlGaN	PCE	–	0.0488	254	[156]
Pt/AlGaN	PCE	–	0.045	254	[157]

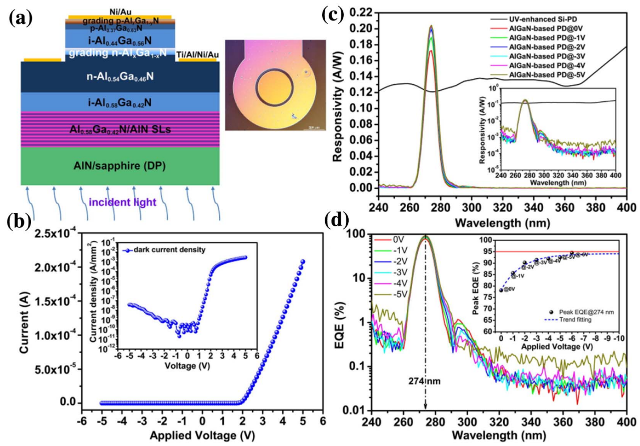

Fig. 10. (a) Schematic and physical images of AlGaN-based p-i-n SBPD. (b) *I-V* curve and the corresponding current density of the device. (c) Spectral responsivity of AlGaN-based p-i-n SBPD under different bias. The inset shows the responsivity plot in semi-log scale. (d) The corresponding EQE in semi-log scale. The inset shows the variation trend of EQE with applied bias. Reproduced with permission[149]. Copyright 2020, Elsevier.

facilitates the separation and transmission of carriers in the SBPD.

Yoshikawa *et al.* reported a type of polarization-assisted $Al_{0.6}Ga_{0.4}N/Al_{0.5}Ga_{0.5}N$ MSM SBPD with high performance[146]. The 2DEG generated at the hetero-interface can provide superior photosensitivity for the SBPD. Upon irradiation with $10\,\mu W/cm^2$, the device exhibited the ultralow dark current of 10^{-11} A and high photocurrent of 5×10^{-5} A at 5 V bias with a cut-off wavelength of 280 nm. In addition, the metal electrode was employed as a Schottky electrode with an appropriate barrier height for the reduced dark current. It is noted that the polarization-assisted SBPD exhibited a rather high responsivity of 10^6 A/W and a rejection ratio of 10^6 under $10\,nW/cm^2$ irradiation. Their work proves that employing the polarization effect can facilitate obtaining AlGaN-based MSM SBPDs with superior photosensitivity.

Kalra *et al.* reported a type of polarization-assisted $Al_{0.4}Ga_{0.6}N$ p-i-n SBPD with an EQE of 92%[95]. The zero-bias responsivity was measured as 211 mA/W at 289 nm, which was a relatively high value reported for AlGaN-based p-i-n SBPDs. The p-i-n SBPD exhibited a low dark current density ($1\,nA\,cm^{-2}$ at 10 V bias), a high response rejection ratio ($>10^6$), and a thermal-noise-limited detectivity ($6.1\times10^{14}\,cm\,Hz^{1/2}\,W^{-1}$). They believed the state-of-the-art performances of the p-i-n SBPD were attributed to high crystalline quality of the AlGaN epilayer resulting from the application of an AlN/AlGaN superlattice buffer layer and an improved p-contact via polarization grading.

Shao *et al*. brought up improved AlGaN APDs SBPDs with the SAM structure, with a polarization electric field whose direction was the same as the reverse bias field in the multiplication region[158]. This polarization electric field could be realized by reducing the Al content of the p-AlGaN layer in a conventional p-i-n-i-n structure. Compared with their conventional counterparts, the polarization-enhanced AlGaN APD SBPDs with an SAM structure exhibited much lower avalanche breakdown voltage. The multiplication gain was up to 2.1×10^4. Moreover, crystalline quality of the polarization-enhanced APD structure was not degraded due to moderated reduction of Al content in the p-AlGaN layer. That guaranteed the polarization-enhanced effect.

4.2. Surface chemical modification

High Al content in AlGaN material will cause poor crystalline quality of the absorption layer and an uneven Schottky barrier resulting from the impurity effect in AlGaN epitaxial film. During the growth of AlGaN, the oxygen impurity is unintentionally introduced into the epitaxial structure. However, the diffusion length of Al atoms is lower than that of Ga atoms in AlGaN film. This increases the affinity of Al to oxidize. There is a possibility of combination of Al atoms and oxygen impurity increasing the Al content in AlGaN film, thereby leading to relatively high density of defects in AlGaN epilayers[159]. Poor crystalline quality of the absorption layer leads to generation of massive carrier trap states at the metal/semiconductor interface[160]. Many photogenerated carriers are captured or recombined at carrier trap states. That results in Fermi level pinning, which can induce lower Schottky barrier height (SBH), thereby decreasing the photodetection efficiency of SBPDs[161]. Therefore, some surface state modification techniques are proposed for high-quality AlGaN materials, including inorganic and organic modification[162–164]. Compared with inorganic molecules, organic molecules used for surface-state chemical modification exhibit ideal occupied and unoccupied molecular orbital levels[98]. Experimental and theoretical studies have demonstrated that organic molecules' modification reconstructs the surface and affects the electrical properties of the surface without actually transferring electrons between the molecules and the substrate. For example, 4,4-triphenyl dithiol, 1,8-octane dithiol, and 1,16-hexadecane dithiol were used for surface modification of GaAs to change its band bending[165]. In addition, ZnTPP (OH), phosphonic acid, can be used to modify the surfaces of Al(Ga)N to change their surface properties[150,166–170].

Recently, Yang *et al.* proposed an organic-modified $Al_{0.6}Ga_{0.4}N$ MSM device structure for solar-blind photodetection[98]. They chose octadecanethiol (ODT) as the modification reagent. The ODT-modified $Al_{0.6}Ga_{0.4}N$ MSM SBPD exhibited a cut-off wavelength of ~250 nm and a weaker dark current in comparison to the same SBPD without ODT modification. The ODT-modified AlGaN SBPD exhibited a relatively high peak responsivity of up to 2.75 A/W at 10 V bias, which was almost three times more than that of the same SBPD without ODT modification. The result could be originated from the fact that ODT molecules could suppress the oxidation of AlGaN surfaces to reduce surface-state density. Except for the photon adsorption layer, the metal electrodes of SBPDs can also be organic-modified to enhance the responsivity of solar-blind UV light. Li and coworkers' work has proved that, as shown in Fig. 11[151].

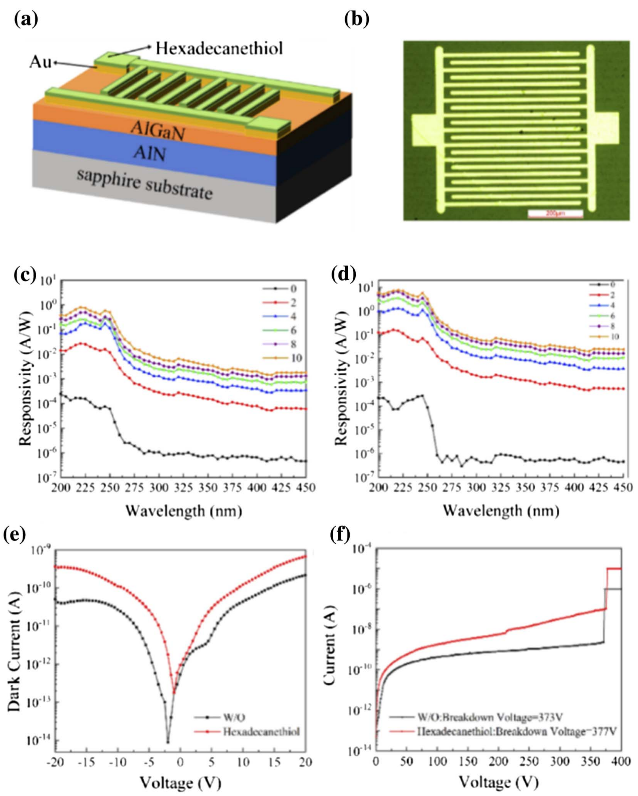

Fig. 11. (a) Schematic structure of HDT-modified AlGaN SBPD. (b) Top-view photograph of HDT-modified AlGaN SBPD. Responsivity of AlGaN SBPD (c) without and (d) with HDT modification at various bias. (e) Dark current of AlGaN SBPD with and without HDT modification. (f) Electrical breakdown characteristics of the AlGaN SBPD with and without HDT modification. Reproduced with permission[151]. Copyright 2021, Optical Society of America.

Hexadecanethiol (HDT) molecules were used as modification reagents and chemically bonded on the metal electrode surface of an $Al_{0.6}Ga_{0.4}N$ MSM SBPD in Figs. 11(a) and 11(b). The SBPD with HDT-modified electrodes exhibited a cut-off wavelength of ~250 nm and a high peak responsivity of 7.598 A/W at 10 V, which was obviously better than the SBPD with unmodified electrodes, as shown in Figs. 11(c) and 11(d). The enhanced peak responsivity of the SBPD with HDT-modified electrodes was attributed to the reduced work function of the metal electrode and change of the SBH owing to the adsorbed HDT. Moreover, *I-V* characteristics were measured from room temperature to 370 K. The results indicated that the HDT modification could also improve the temperature tolerance of the device, which is beneficial for HT solar-blind photodetection.

4.3. Localized surface plasmon resonance

A surface plasmon is an optical phenomenon that involves collective oscillation of charges confined in a nanostructured metal system. When the frequencies of the free electrons on the metal surface and the photons in the incident light wave match each other, a surface-state-excited escaping wave will be generated by collective oscillation. The phenomenon is called surface plasmon resonance. It will propagate along the metal/dielectric interface in the form of vibrating electromagnetic waves. Its amplitude decays exponentially in the direction that is vertical to the metal/dielectric interface. The surface plasmon can be divided into surface plasmon polariton (SPP) and local surface plasmon resonance (LSPR) based on the propagation distance of the electromagnetic wave. When the propagation distance of the electromagnetic wave is greater than the spacing between metal particles, the evanescent wave can propagate between metals, which is called SPP. On the contrary, if the propagation distance is smaller than the spacing between metal particles, the electromagnetic wave cannot propagate between metal particles, which is called LSPR. According to the characteristics of SPP and LSPR, it is known that the SPP usually exists in the interface between metal and dielectric films and propagates along the continuous metal film surface, while the LSPR is restricted around discrete metal nanostructures. SPP and LSPR can both improve the optoelectronic performance of the semiconductor device, especially because the LSPR is more widely used in photodetectors.

Generally, Ag and Au nanoparticles (NPs) are ideal candidates for improving the performance of optoelectronic devices[171,172]. However, the plasmon frequencies of these metals are less than the frequency of solar-blind UV light, so they are not suitable for further application in SBPDs[173]. Zhang *et al.* found that the plasmon frequency of Al NPs could match with that of solar-blind UV light, and they realized remarkable plasmon resonance on $Al_{0.54}Ga_{0.46}N$ MSM SBPDs[153]. The plasmonic-enhanced SBPD exhibited a peak responsivity of 2.34 A/W at 269 nm under 20 V bias, which was 25 times higher than that of the same SBPD without Al NPs. The Al NPs could not only facilitate achieving enhanced responsivity but also well suppress the dark current of the MSM SBPDs. These merits were deemed to originate from the combination of the strong local resonance electric field, the light trapping process, and the passivation effect of the Al NPs.

In addition, Bao *et al.*[99] investigated the effect of Al NPs size on the surface plasmon resonance to find the optimal size of Al NPs for the device. They fabricated a series of AlGaN SBPDs with Al NPs of 20–60 nm. The peak responsivity of 0.288 A/W was achieved in the SBPD with 60 nm Al NPs at 5 V bias, which was two times greater than that in the SBPD without Al NPs. The finite-difference time-domain (FDTD) simulations could be used to theoretically elucidate the reason why the improvement on the SBPDs was ascribed to the LSPR effect of the Al NPs with optimal size. The results are promising for widespread application of AlGaN SBPDs.

Kaushik *et al.* reported a type of LSPR-enhanced $Al_{0.4}Ga_{0.6}N$ MSM SBPD with strong HT robustness, as shown in Fig. 12[155]. In the study, they utilized the LSPR effect in palladium (Pd) NPs to prominently improve the photosensitivity of $Al_{0.4}Ga_{0.6}N$ MSM SBPDs, and the device also exhibited strong thermal robustness. It is found that the LSPR effect resulting from Pd NPs can lead to a remarkable enhancement by nearly 600%, 300%, and 462% in the photo-to-dark current ratio (PDCR), responsivity, and specific detectivity of the SBPD, respectively,

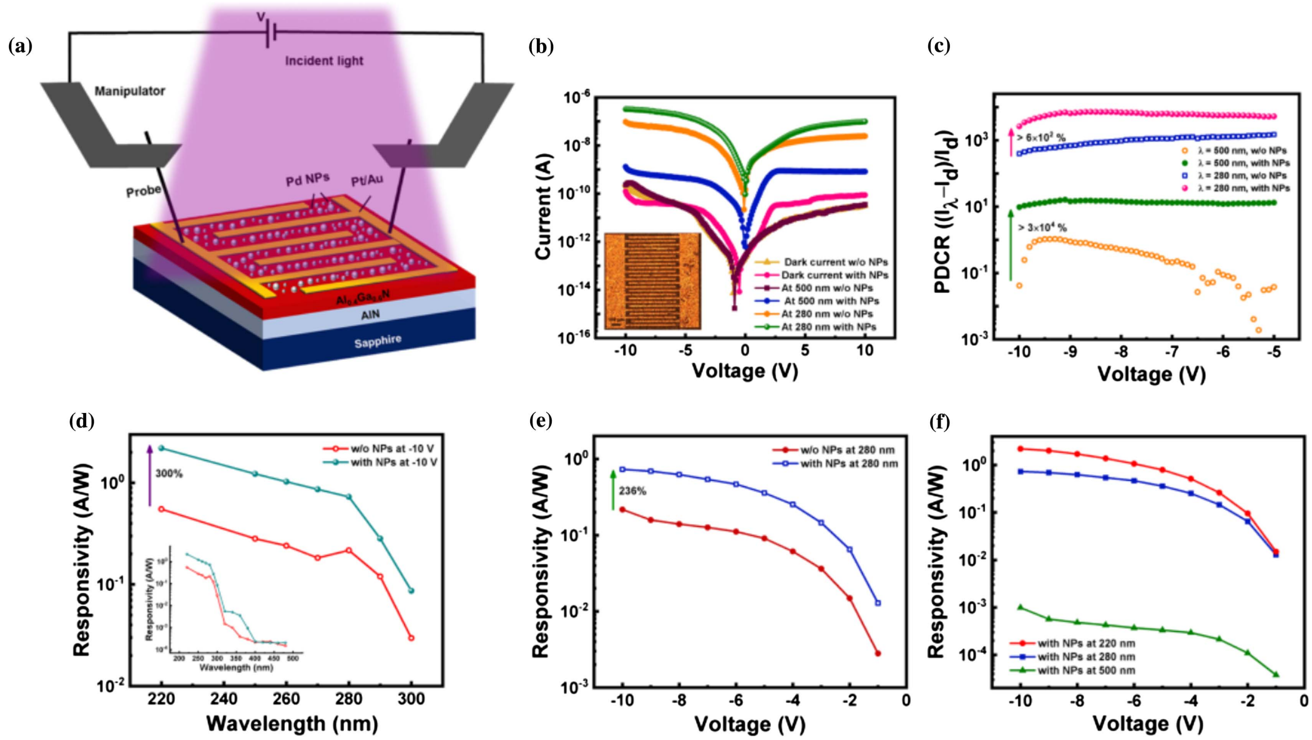

Fig. 12. (a) Schematic illustration of Pd-decorated $Al_{0.4}Ga_{0.6}N$ MSM SBPD. (b) *I–V* characteristics of $Al_{0.4}Ga_{0.6}N$ MSM SBPD with and without Pd NPs in the dark and in the 280/500 nm irradiation. The inset shows the top-view image of the $Al_{0.4}Ga_{0.6}N$ MSM SBPD. (c) PDCR-*V* characteristics for the incident wavelength of 500 and 280 nm for the $Al_{0.4}Ga_{0.6}N$ MSM SBPD with and without Pd NPs. (d) Responsivity spectra of $Al_{0.4}Ga_{0.6}N$ solar-blind PD with and without Pd NPs at -10 V with incident wavelength from 220 to 300 nm. The inset shows the variation in a broad spectral range from 220 to 500 nm. (e) Responsivity spectra of $Al_{0.4}Ga_{0.6}N$ solar-blind PD with and without Pd NPs in the 280 nm irradiation at different voltages. (f) The plot of responsivity with voltage at 500, 280, and 220 nm for Pd-decorated $Al_{0.4}Ga_{0.6}N$ MSM SBPD. Reproduced with permission[155]. Copyright 2022, Institute of Physics.

as shown in Figs. 12(b)–12(e). Under the 280 nm irradiation of $32\ \mu W\ cm^{-2}$ at -10 V, the PDCR, responsivity, and specific detectivity of $Al_{0.4}Ga_{0.6}N$ MSM SBPDs all reach the maximum values of $\sim 3\times 10^3$, 2.7 A/W, and $2.4\times 10^{13}\ cm\ Hz^{1/2}\ W^{-1}$, respectively. The experimental observations are supported by FDTD simulations, which clearly indicate the presence of the LSPR effect in Pd NPs decorated on the surface of the $Al_{0.4}Ga_{0.6}N$ epilayer. The mechanism behind the remarkable enhancement is ascribed to the LSPR-induced effects, namely, improved optical absorption, enhanced local electric field, and LSPR sensitization effect. Moreover, the SBPD exhibited a stable operation up to 400 K, thereby exhibiting the HT robustness desirable for commercial applications.

4.4. Photoelectrochemical cells

Photoelectrochemical UV photodetectors (PEC-UVPDs) have attracted much attention[174]. We use TiO_2, a representative semiconductor material, as an example to elucidate the working mechanism of the PEC-UVPDs in Fig. 13[175]. When the GaN p-n nanowire arrays are illuminated by solar-blind UV light, the absorbed photons will promote photogenerated electrons (e^-_{CB}) migrating from the valence band to the conduction band, leaving behind holes (H^+_{VB}) in the valence band. Then, the photogenerated H^+_{VB} migrate to the semiconductor/electrolyte interface and are captured by electron donors (D) in the electrolyte, forming the oxidized redox species (D^+). Photogenerated e^-_{CB} will transfer from the nanowire arrays to the transparent conductive oxide electrode through external circuits. The formed D^+ in the electrolyte will reach the counter electrode and be recombined by e^-_{CB} from external circuits. Therefore, it suggests that the light harvesting and photogenerated carrier transport simultaneously occur in PEC-UVPDs.

PEC-UVPDs exhibit much higher responsivity and lower fabrication cost in comparison to the reported p-n or Schottky SBPDs. The current output signals of most p-n or Schottky UVPDs range in nano-ampere (nA) order, while those of

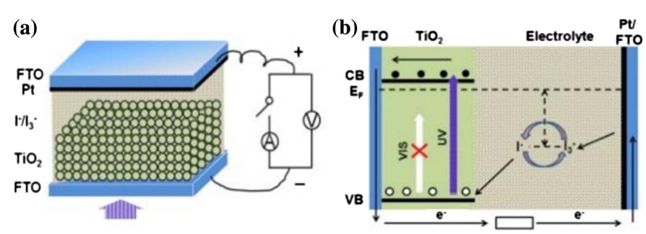

Fig. 13. (a) Schematic of TiO_2 PEC-UVPDs. (b) Energetics of operation of TiO_2 PEC-UVPDs. Reproduced with permission[175]. Copyright 2012, Elsevier.

PEC-SBPDs range in micro-ampere (μA) order. In addition, PEC-UVPDs are usually fabricated via a physicochemical route, cutting down fabrication cost. The excellent merits of PEC-UVPDs brought a promising future for the development of fast photo-responsive, highly spectral-responsive, and highly photosensitive UVPDs with low fabrication cost and self-powering.

However, when it comes to the solar-blind spectral range, those key characteristics of PEC-UVPDs are severely downgraded, hindering further development of high-performance and low-cost photoelectrochemical SBPDs (PEC-SBPDs). Considering the systemically poor photoresponse of PEC-SBPDs, introducing electrocatalysts into the PEC-SBPDs is a reasonable solution to improve the solar-blind UV photoresponse of PEC-SBPDs[176]. The electrocatalysts, especially noble metals like Pt, Ru, and Pd, can vastly promote the photoelectrochemical reactions processing, which will enhance the sensitivity of PEC-SBPDs[156,176,177]. For example, Wang *et al.* reported vertically aligned PEC-SBPDs based on Pt-decorated AlGaN/GaN p-n heterojunction nanowires in electrolytes[178]. They found that the AlGaN/GaN PEC-SBPD exhibited a solar-blind UV photoresponse, in which the photocurrent polarity was reversed depending on the wavelength of light. The device exhibited a negative responsivity of 175 mA/W and a positive responsivity of 31 mA/W under 254 nm and 365 nm illumination at zero bias, respectively. The bipolar photoconductivity behavior was deemed to result from the different redox reactions at the nanowire/electrolyte interface depending on the wavelength of radiation light.

Then, the same research group fabricated a novel type of self-powered AlGaN-based PEC-SBPD, as shown in Fig. 14[157]. After Pt decoration, the Pt/AlGaN PEC-SBPD exhibited effective carrier separation and fast interfacial kinetics, thereby leading to a relatively high responsivity of 45 mA/W and a record response/recovery time of 47/20 ms without an external power

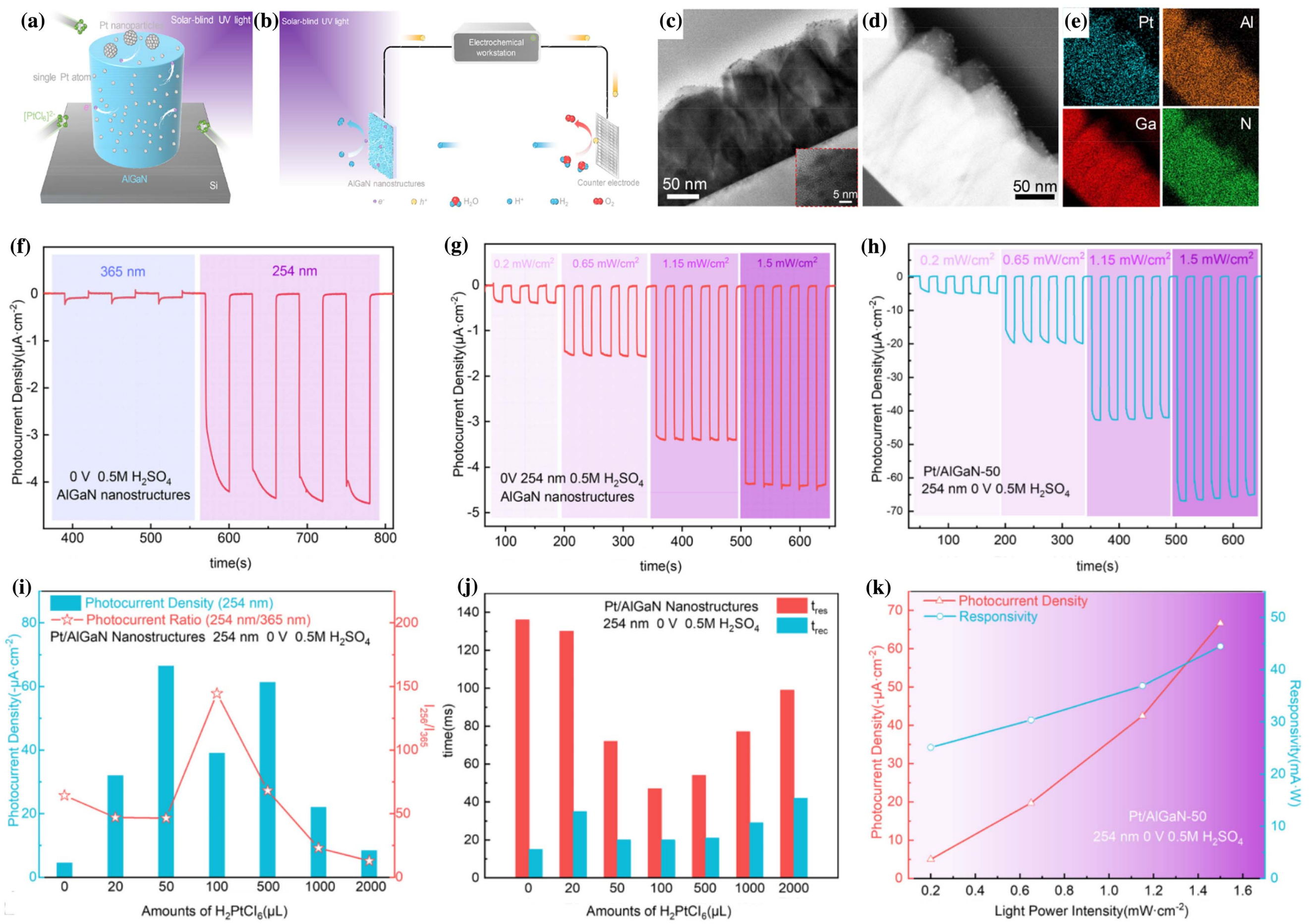

Fig. 14. Schematic illustrations of (a) Pt/AlGaN nanostructures on Si and (b) self-powered Pt/AlGaN PEC-SBPDs. (c)–(e) TEM images and STEM-EDS elemental mapping of Pt/AlGaN-50 nanostructures. Photocurrent densities of AlGaN nanostructures (f) at UV radiation of 254 and 365 nm and (g) at different incident 254 nm solar-blind light intensities. (h) Photocurrent densities of Pt/AlGaN-50 nanostructures at different incident light power intensities. (i) Photocurrent densities and ratios of Pt/AlGaN nanostructures with various Pt loading amounts. (j) Response and recovery time of Pt/AlGaN PEC-SBPDs with different Pt loading amounts. (k) Photocurrent densities and responsivities of Pt/AlGaN-50 nanostructures at different incident light power intensities. Reproduced with permission[157]. Copyright 2020, American Chemical Society.

source. The outstanding results indicate that the combination of using photoelectrochemical cells and loading appropriate electrocatalysts provides a promising future for designing high-performance and self-powered AlGaN SBPDs.

4.5. Monolithic integration

Monolithic integration of DUV LEDs with photodetectors can facilitate achieving high-performance at the system level. The system-level enhancement originates from the integrated design and device ecosystem, which is also named "systems on a chip"[179–184]. For example, Wang *et al.* designed a kind of integrated device composed of an AlGaN-based DUV LED and a multiplicative photoelectric converter (MPC), as shown in Fig. 15[182]. The integrated device can be labeled MPC-DUV LED. In AlGaN-based DUV LEDs, the asymmetrical distribution in electron and hole concentrations will severely degrade the device efficiency. When integrated with a multiplicative p-i-n GaN UV MPC in this paper, the photogenerated holes in the MPC will be injected into the MQWs of AlGaN DUV LEDs under applied voltage. That can balance the carrier distribution in the AlGaN DUV. The device structure and rebalance of carrier concentrations are shown in Fig. 15(a). Consequently, carrier rebalance creates a more uniform hole concentration in the active region of MPC-DUV LEDs, thereby leading to more effective radiative recombination in comparison to that of the conventional DUV LED. Benefitting from the interaction between the p-i-n GaN-based UV MPC and AlGaN-based DUV LED, the MPC-DUV LED exhibits a record wall plug efficiency of 21.6%. This technique is expected to promote the development of high-response photodetectors and high-efficiency light emitters.

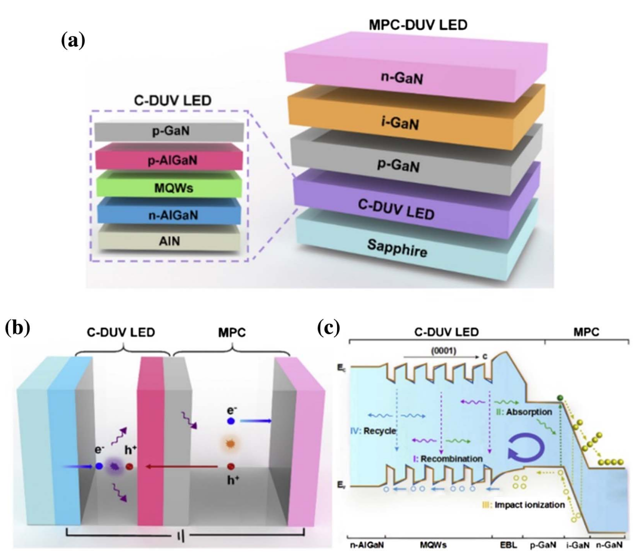

Fig. 15. Schematic diagrams of (a) MPC-DUV LED, (b) carrier recombination and generation in MPC-DUV LED, and (c) photon recycle, gain, and output process in the MPC-DUV LED. Reproduced with permission[182]. Copyright 2019, Elsevier.

5. Conclusion and Outlook

Considerable development has been realized in AlGaN SBPDs over the past two decades. However, there are also bottlenecks hindering the performances of these devices for more advanced applications. The biggest one is the achievement of high-quality AlGaN epilayers as the absorption layers of SBPDs. One effective method is to employ the AlN template because single-crystal AlN templates can mitigate serious lattice mismatches. Nevertheless, bulk single-crystal AlN templates are not widely applied in massive production owing to their high cost. Therefore, AlN/sapphire templates are chosen for their better cost performance compared with bulk single-crystal AlN templates. To further improve the crystalline quality of AlN/sapphire templates, several ingenious construction factors are introduced into AlN epitaxial films, including high–low V/III ratio, SLs, HTA, and embedded voids via PALE methods.

Achieving the high-quality AlGaN films is the first step for fabrication of high-performance SBPDs. Structural design and fabrication processes also exert a strong influence on photodetection properties. Considering the compatibility between mass production and photodetection performance, various types of photovoltaic AlGaN photodiodes, including Schottky barrier, MSM, p-n/p-i-n junctions, and APD, are suitable for SBPDs. Surface engineering techniques, including chemical passivation of surface state, SPP, and LSPR, can be used to further enhance the solar-blind UV photoresponse of AlGaN-based devices. Furthermore, photoelectrochemical cell systems are used for high-speed solar-blind UV photoresponse. That is because the electrocatalysts in the cells can facilitate photoelectrochemical reactions processing, thereby enhancing the sensitivity of AlGaN PEC-SBPDs.

Massive achievements have been realized on solar-blind UV photodetection based on AlGaN materials. However, there are still many challenges that impede the further development of commercialized AlGaN SBPDs. One of the biggest bottlenecks for achieving high-responsivity and low-noise AlGaN SBPDs is the crystalline quality of the AlGaN epitaxial structure with high Al content. Due to the high sticking coefficient of Al atoms, the impurity cannot be avoided during the device manufacturing process. Many ingenious and thoughtful techniques have been proposed to overcome the problems in this manuscript, including AlN buffers with high/low V/III ratio, SL strain relaxation layer, PALE, ELO, HT annealing buffers, and PSS technology, and have substantively decreased the dislocation density of the AlGaN epitaxial structure, thereby enhancing the photosensitivity of AlGaN-based SBPDs.

Template technology also has a strong influence on the evolution of AlGaN SBPDs. Bulk AlN single-crystal substrates can remarkably ameliorate serious lattice mismatches at the AlGaN/AlN interface, which leads to high-quality epitaxial layers with low dislocation density below $5 \times 10^8\ cm^{-2}$. In addition, high thermal conductivity of bulk AlN single-crystal substrates can relieve thermal accumulation effect, thus improving the life span of the device. However, bulk AlN single-crystal substrates suffer from negative influence resulting from high-impurity absorption, high cost, and limited availability. These disadvantages are fatal for the commercialization of bulk AlN substrates. Using the AlN/sapphire template is an eclectic but promising way to fabricate high-quality AlGaN films combined with the ELO technique.

In order to further realize high-quality AlGaN materials, certain challenges, including improving the growth chamber and optimizing the growth conditions, must be conquered. In addition, low doping efficiency of Mg during the fabrication of p-AlGaN leads to serious crystal quality problems. The aforementioned have been developed to suppress the self-compensation process of Mg atoms and reduce the AE of the Mg acceptor in AlGaN. However, simultaneous achievement of high hole concentration and high-quality p-AlGaN alloys still needs more research efforts and better solutions.

In terms of the configuration of AlGaN SBPDs, p-i-n photodiodes, APDs, and phototransistors are promising in the future of solar-blind photodetection. These p-i-n and APDs are ideal candidates of pixel devices of the focal plane array (FPA) used for solar-blind UV image formation. For example, solar-blind FPAs with maximum 320×256 pixels have been realized with the use of AlGaN p-i-n photodiodes, and their application as solar-blind cameras has also been demonstrated[185]. Phototransistors are gate-bias-dependent and highly photosensitive, which provides more possibilities for integration with large-scale integration circuits, thereby facilitating the development of solar-blind non-line-of-sight communication. Further application of the Schottky barrier and MSM photodiodes is restricted by their intrinsic weak points. However, it does not mean that these two types of photodiodes are totally useless in the field of solar-blind photodetection. The fabrication of the Schottky barrier and MSM photodiodes is very simple so that they can be used in the field that does not require high-accuracy solar-blind photodetection, such as flame monitoring. In addition, some new concepts such as plasmonic technologies and surface modification methods can further improve the solar-blind photosensitivity of the Schottky barrier and MSM photodiodes, thereby facilitating their further application. Photoelectrochemical cells used for solar-blind photodetection are very special because they are composed of electrocatalytic chemistry and solar-blind photodetection, which gives the PCE-SBPDs self-powered characteristics. The specific configuration of PCE-SBPDs determines that they can play key roles in some specific fields, such as in-water communication, which is also reported in previous papers[186]. In practice, the compatibility between device configurations, fabrication processes, and operation conditions should be taken into consideration during the fabrication of AlGaN SBPDs.

Although there are many hurdles that exist in this field, we cannot deny that high-Al-content AlGaN alloys still are the most promising candidates of commercialized SBPDs. Recent decades have envisioned the great progress on AlGaN-based SBPDs. Future research work should further concentrate on improving the crystalline quality of the absorption epitaxial layer and optimizing device configurations of SBPDs. In addition, the achieving of effective p-type doping is also important for rational designs of novel conceptual devices. The design of future AlGaN SBPDs should focus on the high response speed, stable repeatability, and reliable reproducibility. With the above successes, the first aim for future work shall be to realize single components of SBPDs with superior performance in comparison to commercially available DUV photodetectors. On the other hand, wafer-scale material uniformity, long-term stability, large-scale integration, environmental friendliness, and cost-effective fabrication of the devices are very pivotal, which requires tremendous research efforts to realize the perspective in blueprints.

Acknowledgement

This work was supported by the National Natural Science Foundation of China (Nos. 52075394 and 51675386), the National Key Research and Development Program of China (No. 2021YFB3600200), and the National Youth Talent Support Program.

References

1. C. Xie, X.-T. Lu, X.-W. Tong, Z.-X. Zhang, F.-X. Liang, L. Liang, L.-B. Luo, and Y.-C. Wu, “Recent progress in solar-blind deep-ultraviolet photodetectors based on inorganic ultrawide bandgap semiconductors,” Adv. Funct. Mater. **29**, 1806006 (2019).
2. J. Chen, W. Ouyang, W. Yang, J.-H. He, and X. Fang, “Recent progress of heterojunction ultraviolet photodetectors: materials, integrations, and applications,” Adv. Funct. Mater. **30**, 1909909 (2020).
3. D. Kaur and M. Kumar, “A strategic review on gallium oxide based deep-ultraviolet photodetectors: recent progress and future prospects,” Adv. Opt. Mater. **9**, 2002160 (2021).
4. A. Kumar, M. A. Khan, and M. Kumar, “Recent advances in 2D materials-based UV photodetectors: a review,” J. Phys. D **55**, 133002 (2021).
5. U. Varshney, N. Aggarwal, and G. Gupta, “Current advances in solar-blind photodetection technology: using Ga_2O_3 & AlGaN,” J. Mater. Chem. C **10**, 1573 (2022).
6. W. Sha, J. Zhang, S. Tan, X. Luo, and W. Hu, “III-nitride piezotronic/piezo-phototronic materials and devices,” J. Phys. D **52**, 213003 (2019).
7. D. Li, K. Jiang, X. Sun, and C. Guo, “AlGaN photonics: recent advances in materials and ultraviolet devices,” Adv. Opt. Photonics **10**, 43 (2018).
8. S. Zhao, J. Lu, X. Hai, and X. Yin, “AlGaN nanowires for ultraviolet light-emitting: recent progress, challenges, and prospects,” Micromachines (Basel) **11**, 125 (2020).
9. E. Iliopoulos and T. D. Moustakas, “Growth kinetics of AlGaN films by plasma-assisted molecular-beam epitaxy,” Appl. Phys. Lett. **81**, 295 (2002).
10. M. E. Coltrin, J. Randall Creighton, and C. C. Mitchell, “Modeling the parasitic chemical reactions of AlGaN organometallic vapor-phase epitaxy,” J. Cryst. Growth **287**, 566 (2006).
11. Q. Cai, H. You, H. Guo, J. Wang, B. Liu, Z. Xie, D. Chen, H. Lu, Y. Zheng, and R. Zhang, “Progress on AlGaN-based solar-blind ultraviolet photodetectors and focal plane arrays,” Light Sci. Appl. **10**, 94 (2021).
12. M. J. Manfra, L. N. Pfeiffer, K. W. West, H. L. Stormer, K. W. Baldwin, J. W. P. Hsu, D. V. Lang, and R. J. Molnar, “High-mobility AlGaN/GaN heterostructures grown by molecular-beam epitaxy on GaN templates prepared by hydride vapor phase epitaxy,” Appl. Phys. Lett. **77**, 2888 (2000).
13. D. Tsvetkov, Y. Melnik, A. Davydov, A. Shapiro, O. Kovalenkov, J. B. Lam, J. J. Song, and V. Dmitriev, “Growth of submicron AlGaN/GaN/AlGaN heterostructures by hydride vapor phase epitaxy (HVPE),” Physica Status Solidi A **188**, 429 (2001).
14. J. Zhao, H. Hu, Y. Lei, H. Wan, L. Gong, and S. Zhou, “Heteroepitaxial growth of high-quality and crack-free AlN film on sapphire substrate with

nanometer-scale-thick AlN nucleation layer for AlGaN-based deep ultraviolet light-emitting diodes," Nanomaterials (Basel) **9**, 1634 (2019).
15. S. V. Averine, P. I. Kuznetzov, V. A. Zhitov, and N. V. Alkeev, "Solar-blind MSM-photodetectors based on $Al_xGa_{1-x}N$/GaN heterostructures grown by MOCVD," Solid State Electron. Lett. **52**, 618 (2008).
16. U. Zeimer, V. Kueller, A. Knauer, A. Mogilatenko, M. Weyers, and M. Kneissl, "High quality AlGaN grown on ELO AlN/sapphire templates," J. Cryst. Growth **377**, 32 (2013).
17. H. Chang, Z. Chen, W. Li, J. Yan, R. Hou, S. Yang, Z. Liu, G. Yuan, J. Wang, J. Li, P. Gao, and T. Wei, "Graphene-assisted quasi-van der Waals epitaxy of AlN film for ultraviolet light emitting diodes on nano-patterned sapphire substrate," Appl. Phys. Lett. **114**, 091107 (2019).
18. S. Sundaram, X. Li, S. Alam, T. Ayari, Y. Halfaya, G. Patriarche, P. L. Voss, J. P. Salvestrini, and A. Ougazzaden, "MOVPE van der Waals epitaxial growth of AlGaN/AlGaN multiple-quantum-well structures with deep UV emission on large scale 2D h-BN buffered sapphire substrates," J. Cryst. Growth **507**, 352 (2019).
19. H. Jeong, M. Cho, Z. Xu, F. Mehnke, M. Bakhtiary-Noodeh, T. Detchprohm, S.-C. Shen, N. Otte, and R. D. Dupuis, "Breakdown characteristics of deep-ultraviolet $Al_{0.6}Ga_{0.4}N$ p-i-n avalanche photodiodes," J. Appl. Phys. **131**, 103102 (2022).
20. L. Gautam, J. Lee, G. Brown, and M. Razeghi, "Low dark current deep UV AlGaN photodetectors on AlN substrate," IEEE J. Quantum Electron. **58**, 4000205 (2022).
21. Y. Chen, Z. Zhang, H. Jiang, Z. Li, G. Miao, and H. Song, "The optimized growth of AlN templates for back-illuminated AlGaN-based solar-blind ultraviolet photodetectors by MOCVD," J. Mater. Chem. C **6**, 4936 (2018).
22. M. Martens, F. Mehnke, C. Kuhn, C. Reich, V. Kueller, A. Knauer, C. Netzel, C. Hartmann, J. Wollweber, J. Rass, T. Wernicke, M. Bickermann, M. Weyers, and M. Kneissl, "Performance characteristics of UV-C AlGaN-based lasers grown on sapphire and Bulk AlN substrates," IEEE Photonics Technol. Lett. **26**, 342 (2014).
23. Y. Chen, C. Zheng, and Y. Chen, "High-performance AlGaN-based solar-blind UV photodetectors for sensing applications," Physica Status Solidi A **218**, 2100207 (2021).
24. K. Lee, R. Page, V. Protasenko, L. J. Schowalter, M. Toita, H. G. Xing, and D. Jena, "MBE growth and donor doping of coherent ultrawide bandgap AlGaN alloy layers on single-crystal AlN substrates," Appl. Phys. Lett. **118**, 092101 (2021).
25. G. Tamulaitis, I. Yilmaz, M. S. Shur, Q. Fareed, R. Gaska, and M. A. Khan, "Photoluminescence of AlGaN grown on bulk AlN substrates," Appl. Phys. Lett. **85**, 206 (2004).
26. H. Amano, R. Collazo, C. D. Santi, S. Einfeldt, M. Funato, J. Glaab, S. Hagedorn, A. Hirano, H. Hirayama, R. Ishii, Y. Kashima, Y. Kawakami, R. Kirste, M. Kneissl, R. Martin, F. Mehnke, M. Meneghini, A. Ougazzaden, P. J. Parbrook, S. Rajan, P. Reddy, F. Römer, J. Ruschel, B. Sarkar, F. Scholz, L. J. Schowalter, P. Shields, Z. Sitar, L. Sulmoni, T. Wang, T. Wernicke, M. Weyers, B. Witzigmann, Y.-R. Wu, T. Wunderer, and Y. Zhang, "The 2020 UV emitter roadmap," J. Phys. D **53**, 503001 (2020).
27. J. Glaab, J. Haefke, J. Ruschel, M. Brendel, J. Rass, T. Kolbe, A. Knauer, M. Weyers, S. Einfeldt, M. Guttmann, C. Kuhn, J. Enslin, T. Wernicke, and M. Kneissl, "Degradation effects of the active region in UV-C light-emitting diodes," J. Appl. Phys. **123**, 104502 (2018).
28. J. Li, N. Gao, D. Cai, W. Lin, K. Huang, S. Li, and J. Kang, "Multiple fields manipulation on nitride material structures in ultraviolet light-emitting diodes," Light Sci. Appl. **10**, 129 (2021).
29. H. Long, J. Dai, Y. Zhang, S. Wang, B. Tan, S. Zhang, L. Xu, M. Shan, Z. C. Feng, H. Kuo, and C. Chen, "High quality 10.6 μm AlN grown on pyramidal patterned sapphire substrate by MOCVD," Appl. Phys. Lett. **114**, 042101 (2019).
30. M. Conroy, V. Z. Zubialevich, H. Li, N. Petkov, J. D. Holmes, and P. J. Parbrook, "Epitaxial lateral overgrowth of AlN on self-assembled patterned nanorods," J. Mater. Chem. C **3**, 431 (2015).
31. T.-Y. Wang, C.-T. Tasi, K.-Y. Lin, S.-L. Ou, R.-H. Horng, and D.-S. Wuu, "Surface evolution and effect of V/III ratio modulation on etch-pit-density improvement of thin AlN templates on nano-patterned sapphire substrates by metalorganic chemical vapor deposition," Appl. Surf. Sci. **455**, 1123 (2018).
32. B. Tang, Z. Wan, H. Hu, L. Gong, and S. Zhou, "Strain management and AlN crystal quality improvement with an alternating V/III ratio AlN superlattice," Appl. Phys. Lett. **118**, 262101 (2021).
33. S. Xiao, K. Shojiki, and H. Miyake, "Thick AlN layers grown on micro-scale patterned sapphire substrates with sputter-deposited annealed AlN films by hydride vapor-phase epitaxy," J. Cryst. Growth **566–567**, 126163 (2021).
34. Y. Iba, K. Shojiki, S. Kuboya, K. Uesugi, S. Xiao, and H. Miyake, "Effect of MOVPE growth conditions on AlN films on annealed sputtered AlN templates with nano-striped patterns," J. Cryst. Growth **570**, 126237 (2021).
35. J. Tajima, Y. Kubota, M. Ishizuki, T. Nagashima, R. Togashi, H. Murakami, Y. Kumagai, K. Takada, and A. Koukitu, "Controlled formation of voids at the AlN/sapphire interface by sapphire decomposition for self-separation of the AlN layer," Physica Status Solidi C **6**, S447 (2009).
36. H. Jiang and T. Egawa, "High quality AlGaN solar-blind Schottky photodiodes fabricated on AIN/sapphire template," Appl. Phys. Lett. **90**, 121121 (2007).
37. C. J. Cheng, J. J. Si, X. F. Zhang, J. X. Ding, Z. X. Lu, W. G. Sun, L. W. Sang, Z. X. Qin, and G. Y. Zhang, "Capacitance characteristics of back-illuminated $Al_{0.42}Ga_{0.58}N/A_{l0.40}Ga_{0.60}N$ heterojunction p-i-n solar-blind UV photodiode," Appl. Phys. Lett. **91**, 253510 (2007).
38. Q. Cai, M. Ge, J. Xue, L. Hu, D. Chen, H. Lu, R. Zhang, and Y. Zheng, "An improved design for solar-blind AlGaN avalanche photodiodes," IEEE Photonics J. **9**, 6803507 (2017).
39. H. You, Z. Shao, Y. Wang, L. Hu, D. Chen, H. Lu, R. Zhang, and Y. Zheng, "Fine control of the electric field distribution in the heterostructure multiplication region of AlGaN avalanche photodiodes," IEEE Photonics J. **9**, 6802007 (2017).
40. S. Zhou, X. Zhao, P. Du, Z. Zhang, X. Liu, S. Liu, and L. J. Guo, "Application of patterned sapphire substrate for III-nitride light-emitting diodes," Nanoscale **14**, 4887 (2022).
41. H. Hu, B. Tang, H. Wan, H. Sun, S. Zhou, J. Dai, C. Chen, S. Liu, and L. J. Guo, "Boosted ultraviolet electroluminescence of InGaN/AlGaN quantum structures grown on high-index contrast patterned sapphire with silica array," Nano Energy **69**, 104427 (2020).
42. G. Parish, S. Keller, P. Kozodoy, J. P. Ibbetson, H. Marchand, P. T. Fini, S. B. Fleischer, S. P. DenBaars, U. K. Mishra, and E. J. Tarsa, "High-performance (Al,Ga)N-based solar-blind ultraviolet p-i-n detectors on laterally epitaxially overgrown GaN," Appl. Phys. Lett. **75**, 247 (1999).
43. C. He, W. Zhao, K. Zhang, L. He, H. Wu, N. Liu, S. Zhang, X. Liu, and Z. Chen, "High-quality GaN epilayers achieved by facet-controlled epitaxial lateral overgrowth on sputtered AlN/PSS templates," ACS Appl. Mater. Interfaces **9**, 43386 (2017).
44. J. Zhang, Y. Yang, and H. Jia, "AlGaN metal-semiconductor-metal ultraviolet photodetectors on sapphire substrate with a low-temperatureAlN buffer layer," Chin. Opt. Lett. **11**, 102304 (2013).
45. C. Pernot, A. Hirano, M. Iwaya, T. Detchprohm, H. Amano, and I. Akasaki, "Solar-blind UV photodetectors based on GaN/AlGaN p-i-n photodiodes," Jpn. J. Appl. Phys. **39**, L387 (2000).
46. M. Brendel, M. Helbling, A. Knauer, S. Einfeldt, A. Knigge, and M. Weyers, "Top- and bottom-illumination of solar-blind AlGaN metal-semiconductor-metal photodetectors," Physica Status Solidi A **212**, 1021 (2015).
47. P. Du, X. Zhao, Y. Qian, P. Liu, B. Tang, L. Shi, G. Tao, and S. Zhou, "Rational superlattice electron blocking layer design for boosting the quantum efficiency of 371 nm ultraviolet light-emitting diodes," IEEE Trans. Electron Devices, **68**, 6255 (2021).
48. S. Zhou, S. Yuan, Y. Liu, L. J. Guo, S. Liu, and H. Ding, "Highly efficient and reliable high-power LEDs with patterned sapphire substrate and strip-shaped distributed current blocking layer," Appl. Surf. Sci. **355**, 1013 (2015).
49. X. Zhao, B. Tang, L. Gong, J. Bai, J. Ping, and S. Zhou, "Rational construction of staggered InGaN quantum wells for efficient yellow light-emitting diodes," Appl. Phys. Lett. **118**, 182102 (2021).
50. S. Zhou, X. Liu, H. Yan, Z. Chen, Y. Liu, and S. Liu, "Highly efficient GaN-based high-power flip-chip light-emitting diodes," Opt. Express **27**, A669 (2019).
51. H. Hu, S. Zhou, X. Liu, Y. Gao, C. Gui, and S. Liu, "Effects of GaN/AlGaN/sputtered AlN nucleation layers on performance of GaN-based ultraviolet light-emitting diodes," Sci. Rep. **7**, 44627 (2017).
52. S. J. Chang, Y. D. Jhou, Y. C. Lin, S. L. Wu, C. H. Chen, T. C. Wen, and L. W. Wu, "GaN-based MSM photodetectors prepared on patterned sapphire substrates," *IEEE Photon. Technol. Lett.* **20**, 1866 (2008).

53. S. J. Chang, S. M. Wang, T. P. Chen, S. J. Young, Y. C. Lin, S. L. Wu, and B. R. Huang, "GaN Schottky barrier photodetectors prepared on patterned sapphire substrate," J. Electrochem. Soc. **157**, J212 (2010).
54. C. K. Wang, Y. Z. Chiou, S. J. Chang, W. C. Lai, S. P. Chang, C. H. Yen, and C. C. Hung, "GaN MSM UV photodetector with sputtered AlN nucleation layer," IEEE Sens. J. **15**, 4743 (2015).
55. S. Hagedorn, S. Walde, N. Susilo, C. Netzel, N. Tillner, R.-S. Unger, P. Manley, E. Ziffer, T. Wernicke, C. Becker, H.-J. Lugauer, M. Kneissl, and M. Weyers, "Improving AlN crystal quality and strain management on nanopatterned sapphire substrates by high-temperature annealing for UVC light-emitting diodes," Physica Status Solidi A **217**, 1900796 (2020).
56. H. Miyake, C.-H. Lin, K. Tokoro, and K. Hiramatsu, "Preparation of high-quality AlN on sapphire by high-temperature face-to-face annealing," J. Cryst. Growth **456**, 155 (2016).
57. M. X. Wang, F. J. Xu, N. Xie, Y. H. Sun, B. Y. Liu, W. K. Ge, X. N. Kang, Z. X. Qin, X. L. Yang, X. Q. Wang, and B. Shen, "High-temperature annealing induced evolution of strain in AlN epitaxial films grown on sapphire substrates," Appl. Phys. Lett. **114**, 112105 (2019).
58. S. Hagedorn, A. Mogilatenko, S. Walde, D. Pacak, J. Weinrich, C. Hartmann, and M. Weyers, "High-temperature annealing and patterned AlN/sapphire interfaces," Physica Status Solidi B **258**, 2100187 (2021).
59. K. Uesugi, Y. Hayashi, K. Shojiki, and H. Miyake, "Reduction of threading dislocation density and suppression of cracking in sputter-deposited AlN templates annealed at high temperatures," Appl. Phys. Express **12**, 065501 (2019).
60. M. Wang, F. Xu, N. Xie, Y. Sun, B. Liu, Z. Qin, X. Wang, and B. J. C. Shen, "Crystal quality evolution of AlN films via high-temperature annealing under ambient N_2 conditions," CrystEngComm **20**, 6613 (2018).
61. O. Reentilä, F. Brunner, A. Knauer, A. Mogilatenko, W. Neumann, H. Protzmann, M. Heuken, M. Kneissl, M. Weyers, and G. Tränkle, "Effect of the AIN nucleation layer growth on AlN material quality," J. Cryst. Growth **310**, 4932 (2008).
62. R. Miyagawa, S. Yang, H. Miyake, K. Hiramatsu, T. Kuwahara, M. Mitsuhara, and N. Kuwano, "Microstructure of AlN grown on a nucleation layer on a sapphire substrate," Appl. Phys Express **5**, 025501 (2012).
63. Y. Itokazu, S. Kuwaba, M. Jo, N. Kamata, and H. Hirayama, "Influence of the nucleation conditions on the quality of AlN layers with high-temperature annealing and regrowth processes," Jpn. J. Appl. Phys. **58**, SC1056 (2019).
64. Y. Chen, H. Song, D. Li, X. Sun, H. Jiang, Z. Li, G. Miao, Z. Zhang, and Y. Zhou, "Influence of the growth temperature of AlN nucleation layer on AlN template grown by high-temperature MOCVD," Mater. Lett. **114**, 26 (2014).
65. M. Balaji, R. Ramesh, P. Arivazhagan, M. Jayasakthi, R. Loganathan, K. Prabakaran, S. Suresh, S. Lourdudoss, and K. Baskar, "Influence of initial growth stages on AlN epilayers grown by metal organic chemical vapor deposition," J. Cryst. Growth **414**, 69 (2015).
66. C. G. Van de Walle and J. Neugebauer, "First-principles calculations for defects and impurities: applications to III-nitrides," J. Appl. Phys. **95**, 3851 (2004).
67. M. Katsuragawa, S. Sota, M. Komori, C. Anbe, T. Takeuchi, H. Sakai, H. Amano, and I. Akasaki, "Thermal ionization energy of Si and Mg in AlGaN," J. Cryst. Growth **189–190**, 528 (1998).
68. H. Tokunaga, A. Ubukata, Y. Yano, A. Yamaguchi, N. Akutsu, T. Yamasaki, and K. Matsumoto, "Effects of growth pressure on AlGaN and Mg-doped GaN grown using multiwafer metal organic vapor phase epitaxy system," J. Cryst. Growth **272**, 348 (2004).
69. G. Namkoong, W. A. Doolittle, and A. S. Brown, "Incorporation of Mg in GaN grown by plasma-assisted molecular beam epitaxy," Appl. Phys. Lett. **77**, 4386 (2000).
70. P. Pampili and P. J. Parbrook, "Doping of III-nitride materials," Mater. Sci. Semicond. Process. **62**, 180 (2017).
71. Y. Chen, H. Wu, E. Han, G. Yue, Z. Chen, Z. Wu, G. Wang, and H. Jiang, "High hole concentration in p-type AlGaN by indium-surfactant-assisted Mg-delta doping," Appl. Phys. Lett. **106**, 162102 (2015).
72. P. Kozodoy, M. Hansen, S. P. DenBaars, and U. K. Mishra, "Enhanced Mg doping efficiency in $Al_{0.2}Ga_{0.8}N$/GaN superlattices," Appl. Phys. Lett. **74**, 3681 (1999).
73. M. L. Nakarmi, K. H. Kim, J. Li, J. Y. Lin, and H. X. Jiang, "Enhanced p-type conduction in GaN and AlGaN by Mg-δ-doping," Appl. Phys. Lett. **82**, 3041 (2003).
74. Y.-J. Ji, Y.-J. Du, and M.-S. Wang, "Electronic structure and optical properties of Al and Mg co-doped GaN," Chin. Phys. B **22**, 117103 (2013).
75. T. C. Zheng, W. Lin, R. Liu, D. J. Cai, J. C. Li, S. P. Li, and J. Y. Kang, "Improved p-type conductivity in Al-rich AlGaN using multidimensional Mg-doped superlattices," Sci. Rep. **6**, 21897 (2016).
76. S. R. Aid, T. Uneme, N. Wakabayashi, K. Yamazaki, A. Uedono, and S. Matsumoto, "Carrier activation in Mg implanted GaN by short wavelength Nd:YAG laser thermal annealing," Physica Status Solidi A **214**, 1700225 (2017).
77. L. Sun, Z. Lv, Z. Zhang, X. Qiu, and H. Jiang, "High-performance AlGaN heterojunction phototransistor with dopant-free polarization-doped P-base," IEEE Electron Device Lett. **41**, 325 (2020).
78. J. Simon, V. Protasenko, C. Lian, H. Xing, and D. Jena, "Polarization-induced hole doping in wide-band-gap uniaxial semiconductor heterostructures," Science **327**, 60 (2010).
79. Z.-H. Zhang, S.-W. Huang Chen, C. Chu, K. Tian, M. Fang, Y. Zhang, W. Bi, and H.-C. Kuo, "Nearly efficiency-droop-free AlGaN-based ultraviolet light-emitting diodes with a specifically designed superlattice p-type electron blocking layer for high Mg doping efficiency," Nanoscale Res. Lett. **13**, 122 (2018).
80. T.-Y. Wang, C.-T. Tasi, C.-F. Lin, and D.-S. Wuu, "85% internal quantum efficiency of 280-nm AlGaN multiple quantum wells by defect engineering," Sci. Rep. **7**, 14422 (2017).
81. A. V. Lobanova, K. M. Mazaev, R. A. Talalaev, M. Leys, S. Boeykens, K. Cheng, and S. Degroote, "Effect of V/III ratio in AlN and AlGaN MOVPE," J. Cryst. Growth **287**, 601 (2006).
82. T. Y. Wang, J. H. Liang, G. W. Fu, and D. S. Wuu, "Defect annihilation mechanism of AlN buffer structures with alternating high and low V/III ratios grown by MOCVD," CrystEngComm **18**, 9152 (2016).
83. S. Hagedorn, A. Knauer, A. Mogilatenko, E. Richter, and M. Weyers, "AlN growth on nano-patterned sapphire: a route for cost efficient pseudo substrates for deep UV LEDs," Physica Status Solidi A **213**, 3178 (2016).
84. L. Zhang, F. Xu, J. Wang, C. He, W. Guo, M. Wang, B. Sheng, L. Lu, Z. Qin, X. Wang, and B. Shen, "High-quality AlN epitaxy on nano-patterned sapphire substrates prepared by nano-imprint lithography," Sci. Rep. **6**, 35934 (2016).
85. B. Tang, H. Hu, H. Wan, J. Zhao, L. Gong, Y. Lei, Q. Zhao, and S. Zhou, "Growth of high-quality AlN films on sapphire substrate by introducing voids through growth-mode modification," Appl. Surf. Sci. **518**, 146218 (2020).
86. N. Biyikli, O. Aytur, I. Kimukin, T. Tut, and E. Ozbay, "Solar-blind AlGaN-based Schottky photodiodes with low noise and high detectivity," Appl. Phys. Lett. **81**, 3272 (2002).
87. N. Biyikli, I. Kimukin, T. Kartaloglu, O. Aytur, and E. Ozbay, "High-speed solar-blind photodetectors with indium-tin-oxide Schottky contacts," Appl. Phys. Lett. **82**, 2344 (2003).
88. S. Butun, T. Tut, B. Butun, M. Gokkavas, H. Yu, and E. Ozbay, "Deep-ultraviolet $Al_{0.75}Ga_{0.25}N$ photodiodes with low cutoff wavelength," Appl. Phys. Lett. **88**, 123503 (2006).
89. S. Muhtadi, S. M. Hwang, A. L. Coleman, A. Lunev, F. Asif, V. S. N. Chava, M. V. S. Chandrashekhar, and A. Khan, "High-speed solar-blind UV photodetectors using high-Al content $Al_{0.64}Ga_{0.36}N/Al_{0.34}Ga_{0.66}N$ multiple quantum wells," Appl. Phys. Express **10**, 011004 (2016).
90. L. Ting, D. J. H. Lambert, M. M. Wong, C. J. Collins, B. Yang, A. L. Beck, U. Chowdhury, R. D. Durpuis, and J. C. Campbell, "Low-noise back-illuminated $Al_xGa_{1-x}N$-based p-i-n solar-blind ultraviolet photodetectors," IEEE J. Quantum Electron. **37**, 538 (2001).
91. N. Biyikli, I. Kimukin, O. Aytur, and E. Ozbay, "Solar-blind AlGaN-based p-i-n photodiodes with low dark current and high detectivity," IEEE Photonics Technol. Lett. **16**, 1718 (2004).
92. V. V. Kuryatkov, B. A. Borisov, S. A. Nikishin, Y. Kudryavtsev, R. Asomoza, V. I. Kuchinskii, G. S. Sokolovskii, D. Y. Song, and M. Holtz, "247 nm solar-blind ultraviolet p-i-n photodetector," J. Appl. Phys. **100**, 096104 (2006).
93. R. McClintock, A. Yasan, K. Mayes, D. Shiell, S. R. Darvish, P. Kung, and M. Razeghi, "High quantum efficiency AlGaN solar-blind p-i-n photodiodes," Appl. Phys. Lett. **84**, 1248 (2004).
94. T. Tut, T. Yelboga, E. Ulker, and E. Ozbay, "Solar-blind AlGaN-based p-i-n photodetectors with high breakdown voltage and detectivity," Appl. Phys. Lett. **92**, 103502 (2008).

95. A. Kalra, S. Rathkanthiwar, R. Muralidharan, S. Raghavan, and D. N. Nath, "Polarization-graded AlGaN solar-blind p-i-n detector with 92% zero-bias external quantum efficiency," IEEE Photonics Technol. Lett. **31**, 1237 (2019).
96. F. Xie, H. Lu, D. Chen, X. Ji, F. Yan, R. Zhang, Y. Zheng, L. Li, and J. Zhou, "Ultra-low dark current AlGaN-based solar-blind metal–semiconductor–metal photodetectors for high-temperature applications," IEEE Sens. J. **12**, 2086 (2012).
97. R. Tan, Q. Cai, J. Wang, D. Pan, Z. Li, and D. Chen, "Highly solar-blind ultraviolet selective metal-semiconductor-metal photodetector based on back-illuminated AlGaN heterostructure with integrated photonic crystal filter," Appl. Phys. Lett. **118**, 142105 (2021).
98. G. Yang, Y. Li, Y. Liu, F. Xie, Y. Gu, X. Yang, C. Wei, B. Bian, X. Zhang, and N. Lu, "Surface modification of AlGaN solar-blind ultraviolet MSM photodetectors with octadecanethiol," *IEEE Trans. Electron Devices* **69**, 195 (2021).
99. G. Bao, D. Li, X. Sun, M. Jiang, Z. Li, H. Song, H. Jiang, Y. Chen, G. Miao, and Z. Zhang, "Enhanced spectral response of an AlGaN-based solar-blind ultraviolet photodetector with Al nanoparticles," Opt. Express **22**, 24286 (2014).
100. L. Sun, J. Chen, J. Li, and H. Jiang, "AlGaN solar-blind avalanche photodiodes with high multiplication gain," Appl. Phys. Lett. **97**, 191103 (2010).
101. Y. Huang, D. J. Chen, H. Lu, K. X. Dong, R. Zhang, Y. D. Zheng, L. Li, and Z. H. Li, "Back-illuminated separate absorption and multiplication AlGaN solar-blind avalanche photodiodes," Appl. Phys. Lett. **101**, 253516 (2012).
102. Z. Huang, J. Li, W. Zhang, and H. Jiang, "AlGaN solar-blind avalanche photodiodes with enhanced multiplication gain using back-illuminated structure," Appl. Phys. Express **6**, 054101 (2013).
103. Z. G. Shao, D. J. Chen, H. Lu, R. Zhang, D. P. Cao, W. J. Luo, Y. D. Zheng, L. Li, and Z. H. Li, "High-gain AlGaN solar-blind avalanche photodiodes," IEEE Electron Device Lett. **35**, 372 (2014).
104. Z. G. Shao, X. F. Yang, H. F. You, D. J. Chen, H. Lu, R. Zhang, Y. D. Zheng, and K. X. Dong, "Ionization-enhanced algan heterostructure avalanche photodiodes," IEEE Electron Device Lett. **38**, 485 (2017).
105. Q. Cai, W. Luo, R. Yuan, H. You, Q. Li, M. Li, D. Chen, H. Lu, R. Zhang, and Y. Zheng, "Back-illuminated AlGaN heterostructure solar-blind avalanche photodiodes with one-dimensional photonic crystal filter," Opt. Express **28**, 6027 (2020).
106. C. J. Cheng, X. F. Zhang, Z. X. Lu, J. X. Ding, L. Zhang, L. Zhao, J. J. Si, W. G. Sun, L. W. Sang, Z. X. Qin, and G. Y. Zhang, "Temperature dependence on current-voltage characteristics of Ni/Au-$Al_{0.45}Ga_{0.55}N$ Schottky photodiode," Appl. Phys. Lett. **92**, 103505 (2008).
107. G. Mazzeo, J. Reverchon, J. Duboz, and A. Dussaigne, "AlGaN-based linear array for UV solar-blind imaging from 240 to 280 nm," IEEE Sens. J. **6**, 957 (2006).
108. S. Rathkanthiwar, A. Kalra, S. V. Solanke, N. Mohta, R. Muralidharan, S. Raghavan, and D. N. Nath, "Gain mechanism and carrier transport in high responsivity AlGaN-based solar blind metal semiconductor metal photodetectors," J. Appl. Phys. **121**, 164502 (2017).
109. Y. Chen, X. Zhou, Z. Zhang, G. Miao, H. Jiang, Z. Li, and H. Song, "Dual-band solar-blind UV photodetectors based on AlGaN/AlN superlattices," Mater. Lett. **291**, 129583 (2021).
110. S. F. Nwabunwanne and W. R. Donaldson, "Boosting the external quantum efficiency of AlGaN-based metal-semiconductor-metal ultraviolet photodiodes by electrode geometry variation," IEEE J. Quantum Electron. **57**, 4000608 (2021).
111. Z. Wang, D. Zhou, W. Xu, D. Pan, F. Ren, D. Chen, R. Zhang, Y. Zheng, and H. Lu, "High-performance 4H-SiC Schottky photodiode with semitransparent grid-electrode for EUV detection," IEEE Photon. Technol. Lett. **32**, 791 (2020).
112. N. Kumar, K. Arora, and M. Kumar, "High performance, flexible and room temperature grown amorphous Ga_2O_3 solar-blind photodetector with amorphous indium-zinc-oxide transparent conducting electrodes," J. Phys. D **52**, 335103 (2019).
113. O. Katz, V. Garber, B. Meyler, G. Bahir, and J. Salzman, "Gain mechanism in GaN Schottky ultraviolet detectors," Appl. Phys. Lett. **79**, 1417 (2001).
114. O. Katz, G. Bahir, and J. Salzman, "Persistent photocurrent and surface trapping in GaN Schottky ultraviolet detectors," Appl. Phys. Lett. **84**, 4092 (2004).
115. S. Rathkanthiwar, A. Kalra, R. Muralidharan, D. N. Nath, and S. Raghavan, "Analysis of screw dislocation mediated dark current in $Al_{0.50}Ga_{0.50}N$ solar-blind metal-semiconductor-metal photodetectors," J. Cryst. Growth **498**, 35 (2018).
116. D. Li, X. Sun, H. Song, Z. Li, Y. Chen, G. Miao, and H. Jiang, "Influence of threading dislocations on GaN-based metal-semiconductor-metal ultraviolet photodetectors," Appl. Phys. Lett. **98**, 011108 (2011).
117. Z. Dai, Y. Liu, G. Yang, F. Xie, C. Zhu, Y. Gu, N. Lu, Q. Fan, Y. Ding, Y. Li, Y. Yu, and X. Zhang, "Carrier transport and photoconductive gain mechanisms of AlGaN MSM photodetectors with high Al Content," Chin. Opt. Lett. **19**, 082504 (2021).
118. M. Brendel, M. Helbling, A. Knigge, F. Brunner, and M. Weyers, "Measurement and simulation of top- and bottom-illuminated solar-blind AlGaN metal-semiconductor-metal photodetectors with high external quantum efficiencies," J. Appl. Phys. **118**, 244504 (2015).
119. Z. Xiaodan, Y. Yibiao, W. Yuncai, H. Yuying, C. Zhihui, and Z. Mingda, "Study of the converter based on photonic crystals filters and quantum dots for solar blind ultraviolet imaging system," Opt. Eng. **57**, 117106 (2018).
120. R. Yuan, H. You, Q. Cai, K. Dong, T. Tao, B. Liu, D. Chen, R. Zhang, and Y. Zheng, "A high-performance SiO_2/SiN_x 1-D photonic crystal UV filter used for solar-blind photodetectors," IEEE Photonics J. **11**, 2201007 (2019).
121. X. Y. Sun, X. H. Chen, J. G. Hao, Z. P. Wang, Y. Xu, H. H. Gong, Y. J. Zhang, X. X. Yu, C. D. Zhang, F.-F. Ren, S. L. Gu, R. Zhang, and J. D. Ye, "A self-powered solar-blind photodetector based on polyaniline/α-Ga_2O_3 p-n heterojunction," Appl. Phys. Lett. **119**, 141601 (2021).
122. M. Jiang, Y. Zhao, L. Bian, W. Yang, J. Zhang, Y. Wu, M. Zhou, S. Lu, and H. Qin, "Self-powered photoelectrochemical (Al,Ga)N photodetector with an ultrahigh ultraviolet/visible reject ratio and a quasi-invisible functionality for 360° omnidirectional detection," ACS Photonics **8**, 3282 (2021).
123. D. G. Zhao, S. Zhang, D. S. Jiang, J. J. Zhu, Z. S. Liu, H. Wang, S. M. Zhang, B. S. Zhang, and H. Yang, "A study on the spectral response of back-illuminated p-i-n AlGaN heterojunction ultraviolet photodetector," J. Appl. Phys. **110**, 053701 (2011).
124. B. Albrecht, S. Kopta, O. John, M. Rütters, M. Kunzer, R. Driad, N. Marenco, K. Köhler, M. Walther, and O. Ambacher, "Improved AlGaN p-i-n photodetectors for monitoring of ultraviolet radiation," IEEE J. Sel. Top. Quantum Electron. **20**, 166 (2014).
125. P. Pramanik, S. Sen, C. Singha, A. S. Roy, A. Das, S. Sen, D. V. S. Rao, and A. Bhattacharyya, "Wavelength-specific ultraviolet photodetectors based on AlGaN multiple quantum wells," IEEE J. Quantum Electron. **52**, 4300206 (2016).
126. L. Guo, K. Jiang, X. Sun, Z. Zhang, J. Ben, Y. Jia, Y. Wang, and D. Li, "Multiple-quantum-well-induced unipolar carrier transport multiplication in AlGaN solar-blind ultraviolet photodiode," Photonics Res. **9**, 1907 (2021).
127. B. Liu, D. Chen, H. Lu, T. Tao, Z. Zhuang, Z. Shao, W. Xu, H. Ge, T. Zhi, F. Ren, J. Ye, Z. Xie, and R. Zhang, "Hybrid light emitters and UV solar-blind avalanche photodiodes based on III-nitride semiconductors," Adv. Mater. **32**, 1904354 (2020).
128. K. Dong, D. Chen, B. Jin, X. Jiang, and J. Shi, "$Al_{0.4}Ga_{0.6}N/Al_{0.15}Ga_{0.85}N$ separate absorption and multiplication solar-blind avalanche photodiodes with a one-dimensional photonic crystal filter," IEEE Photonics J. **8**, 6804307 (2016).
129. Q. Cai, Q. Li, M. Li, Y. Tang, J. Wang, J. Xue, D. Chen, H. Lu, R. Zhang, and Y. Zheng, "Performance modulation for back-illuminated AlGaN ultraviolet avalanche photodiodes based on multiplication scaling," IEEE Photonics J. **11**, 6801507 (2019).
130. Q. Cai, W. Luo, H. Guo, J. Wang, Y. Tang, J. Xue, Q. Li, M. Li, D. Chen, H. Lu, R. Zhang, and Y. Zheng, "Direct observation of reach-through behavior in back-illuminated AlGaN avalanche photodiode with separate absorption and multiplication structure," J. Phys. D **53**, 425101 (2020).
131. R. McClintock, A. Yasan, K. Minder, P. Kung, and M. Razeghi, "Avalanche multiplication in AlGaN based solar-blind photodetectors," Appl. Phys. Lett. **87**, 241123 (2005).
132. L. Hahn, F. Fuchs, L. Kirste, R. Driad, F. Rutz, T. Passow, K. Köhler, R. Rehm, and O. Ambacher, "Avalanche multiplication in AlGaN-based heterostructures for the ultraviolet spectral range," Appl. Phys. Lett. **112**, 151102 (2018).
133. C. Yao, X. Ye, R. Sun, G. Yang, J. Wang, Y. Lu, P. Yan, J. Cao, and S. Gao, "High-performance AlGaN-based solar-blind avalanche photodiodes with

dual-periodic III-nitride distributed Bragg reflectors," Appl. Phys. Express **10**, 034302 (2017).
134. J. Chang, D. Chen, L. Yang, Y. Liu, K. Dong, H. Lu, R. Zhang, and Y. Zheng, "High-quality crystal growth and characteristics of AlGaN-based solar-blind distributed Bragg reflectors with a tri-layer period structure," Sci. Rep. **6**, 29571 (2016).
135. L. Zhang, K. Dong, D. Chen, Y. Liu, J. Xue, H. Lu, R. Zhang, and Y. Zheng, "Solar-blind ultraviolet AlInN/AlGaN distributed Bragg reflectors," Appl. Phys. Lett. **102**, 242112 (2013).
136. M. Abid, T. Moudakir, G. Orsal, S. Gautier, A. En Naciri, Z. Djebbour, J. H. Ryou, G. Patriarche, L. Largeau, H. J. Kim, Z. Lochner, K. Pantzas, D. Alamarguy, F. Jomard, R. D. Dupuis, J. P. Salvestrini, P. L. Voss, and A. Ougazzaden, "Distributed Bragg reflectors based on diluted boron-based BAlN alloys for deep ultraviolet optoelectronic applications," Appl. Phys. Lett. **100**, 051101 (2012).
137. K. Jiang, X. Sun, Y. Chen, S. Zhang, J. Ben, Y. Chen, Z.-H. Zhang, Y. Jia, Z. Shi, and D. Li, "Three-dimensional metal-semiconductor-metal bipolar ultraviolet phototransistor based on GaN p-i-n epilayer," Appl. Phys. Lett. **119**, 161105 (2021).
138. C.-J. Lee, Y.-J. Kwon, C.-H. Won, J.-H. Lee, and S.-H. Hahm, "Dual-wavelength sensitive AlGaN/GaN metal-insulator-semiconductor-insulator-metal ultraviolet sensor with balanced ultraviolet/visible rejection ratios," Appl. Phys. Lett. **103**, 111110 (2013).
139. W. Y. Han, Z. W. Zhang, Z. M. Li, Y. R. Chen, H. Song, G. Q. Miao, F. Fan, H. F. Chen, Z. Liu, and H. Jiang, "High performance back-illuminated MIS structure AlGaN solar-blind ultraviolet photodiodes," J. Mater. Sci. Mater. Electron. **29**, 9077 (2018).
140. A. M. Armstrong, B. Klein, A. A. Allerman, E. A. Douglas, A. G. Baca, M. H. Crawford, G. W. Pickrell, and C. A. Sanchez, "Visible-blind and solar-blind detection induced by defects in AlGaN high electron mobility transistors," J. Appl. Phys. **123**, 114502 (2018).
141. S. Muhtadi, S. Hwang, A. Coleman, F. Asif, A. Lunev, M. V. S. Chandrashekhar, and A. Khan, "Selective area deposited n-$Al_{0.5}Ga_{0.5}N$ channel field effect transistors with high solar-blind ultraviolet photo-responsivity," Appl. Phys. Lett. **110**, 171104 (2017).
142. Y. Yamamoto, A. Yoshikawa, T. Kusafuka, T. Okumura, M. Iwaya, T. Takeuchi, S. Kamiyama, and I. Akasaki, "Realization of high-performance hetero-field-effect-transistor-type ultraviolet photosensors using p-type GaN comprising three-dimensional island crystals," Jpn. J. Appl. Phys. **55**, 05FJ07 (2016).
143. M. Iwaya, S. Miura, T. Fujii, S. Kamiyama, H. Amano, and I. Akasaki, "High-performance UV detector based on AlGaN/GaN junction heterostructure-field-effect transistor with a p-GaN gate," Physica Status Solidi C **6**, S972 (2009).
144. H. Zhang, F. Liang, K. Song, C. Xing, D. Wang, H. Yu, C. Huang, Y. Sun, L. Yang, X. Zhao, H. Sun, and S. Long, "Demonstration of AlGaN/GaN-based ultraviolet phototransistor with a record high responsivity over 3.6 × 107 A/W," Appl. Phys. Lett. **118**, 242105 (2021).
145. L. Yang, H. Zhang, Y. Sun, K. Hu, Z. Xing, K. Liang, S. Fang, D. Wang, H. Yu, Y. Kang, and H. Sun, "Temperature-dependent photodetection behavior of AlGaN/GaN-based ultraviolet phototransistors," Appl. Phys. Lett. **120**, 091103 (2022).
146. A. Yoshikawa, S. Ushida, K. Nagase, M. Iwaya, T. Takeuchi, S. Kamiyama, and I. Akasaki, "High-performance solar-blind $Al_{0.6}Ga_{0.4}N/Al_{0.5}Ga_{0.5}N$ MSM type photodetector," Appl. Phys. Lett. **111**, 191103 (2017).
147. K. Jiang, X. Sun, Z.-H. Zhang, J. Ben, J. Che, Z. Shi, Y. Jia, Y. Chen, S. Zhang, W. Lv, and D. Li, "Polarization-enhanced AlGaN solar-blind ultraviolet detectors," Photonics Res. **8**, 1243 (2020).
148. J. Wang, C. Chu, K. Tian, J. Che, H. Shao, Y. Zhang, K. Jiang, Z.-H. Zhang, X. Sun, and D. Li, "Polarization assisted self-powered GaN-based UV photodetector with high responsivity," Photonics Res. **9**, 734 (2021).
149. Y. Chen, Z. Zhang, G. Miao, H. Jiang, Z. Li, and H. Song, "Epitaxial growth of polarization-graded AlGaN-based solar-blind ultraviolet photodetectors on pre-grown AlN templates," Mater. Lett. **281**, 128638 (2020).
150. S. Kaushik, T. R. Naik, A. Alka, M. Garg, B. R. Tak, M. Ravikanth, V. R. Rao, and R. Singh, "Surface modification of AlN using organic molecular layer for improved deep UV photodetector performance," ACS Appl. Electron. Mater. **2**, 739 (2020).
151. Y. Li, Y. Liu, G. Yang, B. Bian, J. Wang, Y. Gu, Q. Fan, Y. Ding, X. Zhang, N. Lu, and G. Chen, "Enhanced performance of high Al-content AlGaN MSM photodetectors by electrode modification using hexadecanethiol," Opt. Express **29**, 5466 (2021).
152. Q. Wen, C. Wang, X. Qiu, Z. Lv, and H. Jiang, "Significant performance improvement of AlGaN solar-blind heterojunction phototransistors by using Na_2S solution-based surface treatment," Appl. Surf. Sci. **591**, 153144 (2022).
153. W. Zhang, J. Xu, W. Ye, Y. Li, Z. Qi, J. Dai, Z. Wu, C. Chen, J. Yin, J. Li, H. Jiang, and Y. Fang, "High-performance AlGaN metal-semiconductor-metal solar-blind ultraviolet photodetectors by localized surface plasmon enhancement," Appl. Phys. Lett. **106**, 021112 (2015).
154. N. Lu, Y. Gu, Y. Weng, Z. Da, and Y. Ding, "Localized surface plasmon enhanced photoresponse of AlGaN MSM solar-blind ultraviolet photodetectors," Mater. Res. Express **6**, 095033 (2019).
155. S. Kaushik, S. Karmakar, P. Bisht, C.-H. Liao, X. Li, R. K. Varshney, B. R. Mehta, and R. Singh, "Localized surface plasmon resonance-enhanced solar-blind $Al_{0.4}Ga_{0.6}N$ MSM photodetectors exhibiting high-temperature robustness," Nanotechnology **33**, 145202 (2022).
156. D. Wang, C. Huang, X. Liu, H. Zhang, H. Yu, S. Fang, B. S. Ooi, Z. Mi, J.-H. He, and H. Sun, "Highly uniform, self-assembled AlGaN nanowires for self-powered solar-blind photodetector with fast-response speed and high responsivity," Adv. Opt. Mater. **9**, 2000893 (2021).
157. D. Wang, X. Liu, S. Fang, C. Huang, Y. Kang, H. Yu, Z. Liu, H. Zhang, R. Long, Y. Xiong, Y. Lin, Y. Yue, B. Ge, T. K. Ng, B. S. Ooi, Z. Mi, J.-H. He, and H. Sun, "Pt/AlGaN nanoarchitecture: toward high responsivity, self-powered ultraviolet-sensitive photodetection," Nano Lett. **21**, 120 (2021).
158. Z. Shao, D. Chen, Y. Liu, H. Lu, R. Zhang, Y. Zheng, L. Li, and K. Dong, "Significant performance improvement in AlGaN solar-blind avalanche photodiodes by exploiting the built-in polarization electric field," IEEE J. Sel. Top. Quantum Electron. **20**, 187 (2014).
159. X. Li, G. Le Gac, S. Bouchoule, Y. El Gmili, G. Patriarche, S. Sundaram, P. Disseix, F. Réveret, J. Leymarie, J. Streque, F. Genty, J. P. Salvestrini, R. D. Dupuis, X. H. Li, P. L. Voss, and A. Ougazzaden, "Structural and optical investigations of AlGaN MQWs grown on a relaxed AlGaN buffer on AlN templates for emission at 280 nm," J. Cryst. Growth **432**, 37 (2015).
160. M. Ding, Z. Guo, X. Chen, X. Ma, and L. Zhou, "Surface/interface engineering for constructing advanced nanostructured photodetectors with improved performance: a brief review," Nanomaterials (Basel) **10**, 362 (2020).
161. P. Reddy, I. Bryan, Z. Bryan, W. Guo, L. Hussey, R. Collazo, and Z. Sitar, "The effect of polarity and surface states on the Fermi level at III-nitride surfaces," J. Appl. Phys. **116**, 123701 (2014).
162. C. Huh, S.-W. Kim, H.-S. Kim, I.-H. Lee, and S.-J. Park, "Effective sulfur passivation of an n-type GaN surface by an alcohol-based sulfide solution," J. Appl. Phys. **87**, 4591 (2000).
163. J. Spradlin, S. Dogan, M. Mikkelson, D. Huang, L. He, D. Johnstone, H. Morkoç, and R. J. Molnar, "Improvement of n-GaN Schottky diode rectifying characteristics using KOH etching," Appl. Phys. Lett. **82**, 3556 (2003).
164. H. Liu, W. Hsu, B. Chou, and Y. Wang, "A simple passivation technique for AlGaN/GaN ultraviolet Schottky barrier photodetector," IEEE Photonics Technol. Lett. **26**, 138 (2014).
165. T. Aqua, H. Cohen, O. Sinai, V. Frydman, T. Bendikov, D. Krepel, O. Hod, L. Kronik, and R. Naaman, "Role of backbone charge rearrangement in the bond-dipole and work function of molecular monolayers," J. Phys. Chem. C **115**, 24888 (2011).
166. M. Garg, T. R. Naik, R. Pathak, V. R. Rao, C.-H. Liao, K.-H. Li, H. Sun, X. Li, and R. Singh, "Effect of surface passivation process for AlGaN/GaN HEMT heterostructures using phenol functionalized-porphyrin based organic molecules," J. Appl. Phys. **124**, 195702 (2018).
167. B. S. Simpkins, S. Hong, R. Stine, A. J. Mäkinen, N. D. Theodore, M. A. Mastro, C. R. Eddy, and P. E. Pehrsson, "Assembly of phosphonic acids on GaN and AlGaN," J. Phys. D **43**, 015303 (2009).
168. F. Li, E. Shishkin, M. A. Mastro, J. K. Hite, C. R. Eddy, J. H. Edgar, and T. Ito, "Photopolymerization of self-assembled monolayers of diacetylenic alkylphosphonic acids on group-III nitride substrates," Langmuir **26**, 10725 (2010).
169. S. J. Wilkins, T. Paskova, and A. Ivanisevic, "Modified surface chemistry, potential, and optical properties of polar gallium nitride via long chained phosphonic acids," Appl. Surf. Sci. **327**, 498 (2015).

170. T. Ito, S. M. Forman, C. Cao, F. Li, C. R. Eddy, M. A. Mastro, R. T. Holm, R. L. Henry, K. L. Hohn, and J. H. Edgar, "Self-assembled monolayers of alkylphosphonic acid on GaN substrates," Langmuir **24**, 6630 (2008).
171. M.-K. Kwon, J.-Y. Kim, B.-H. Kim, I.-K. Park, C.-Y. Cho, C. C. Byeon, and S.-J. Park, "Surface-plasmon-enhanced light-emitting diodes," Adv. Mater. **20**, 1253 (2008).
172. I. M. Pryce, D. D. Koleske, A. J. Fischer, and H. A. Atwater, "Plasmonic nanoparticle enhanced photocurrent in GaN/InGaN/GaN quantum well solar cells," Appl. Phys. Lett. **96**, 153501 (2010).
173. Y. Wu, X.-J. Sun, Y.-P. Jia, and D.-B. Li, "Review of improved spectral response of ultraviolet photodetectors by surface plasmon," Chin. Phys. B **27**, 126101 (2018).
174. J. Zhou, L. Chen, Y. Wang, Y. He, X. Pan, and E. Xie, "An overview on emerging photoelectrochemical self-powered ultraviolet photodetectors," Nanoscale **8**, 50 (2016).
175. X. Li, C. Gao, H. Duan, B. Lu, X. Pan, and E. Xie, "Nanocrystalline TiO_2 film based photoelectrochemical cell as self-powered UV-photodetector," Nano Energy **1**, 640 (2012).
176. S. Fang, D. Wang, X. Wang, X. Liu, Y. Kang, H. Yu, H. Zhang, W. Hu, J.-H. He, H. Sun, and S. Long, "Tuning the charge transfer dynamics of the nanostructured GaN photoelectrodes for efficient photoelectrochemical detection in the ultraviolet band," Adv. Funct. Mater. **31**, 2103007 (2021).
177. J. Cheng, X. Xuan, X. Yang, J. Zhou, and K. Cen, "Selective reduction of CO_2 to alcohol products on octahedral catalyst of carbonized Cu(BTC) doped with Pd nanoparticles in a photoelectrochemical cell," Chem. Eng. J. **358**, 860 (2019).
178. D. Wang, X. Liu, Y. Kang, X. Wang, Y. Wu, S. Fang, H. Yu, M. Memon, H. Zhang, W. Hu, Z. Mi, L. Fu, H. Sun, and S. Long, "Bidirectional photocurrent in p–n heterojunction nanowires," Nat. Electron. **4**, 645 (2021).
179. C. Huang, H. Zhang, and H. Sun, "Ultraviolet optoelectronic devices based on AlGaN-SiC platform: towards monolithic photonics integration system," Nano Energy **77**, 105149 (2020).
180. C. Liu, Y. Cai, H. Jiang, and K. M. Lau, "Monolithic integration of III-nitride voltage-controlled light emitters with dual-wavelength photodiodes by selective-area epitaxy," Opt. Lett. **43**, 3401 (2018).
181. K. H. Li, H. Lu, W. Y. Fu, Y. F. Cheung, and H. W. Choi, "Intensity-stabilized LEDs with monolithically integrated photodetectors," IEEE Trans. Ind. Electron. **66**, 7426 (2019).
182. S. Wang, H. Long, Y. Zhang, Q. Chen, J. Dai, S. Zhang, J. Chen, R. Liang, L. Xu, F. Wu, Z.-H. Zhang, H. Sun, C. Chen, and Y. Gao, "Monolithic integration of deep ultraviolet LED with a multiplicative photoelectric converter," Nano Energy **66**, 104181 (2019).
183. L. Chen, X. An, J. Jing, H. Jin, Z. Chu, and K. H. Li, "Ultracompact chip-scale refractometer based on an InGaN-based monolithic photonic chip," ACS Appl. Mater. Interfaces **12**, 49748 (2020).
184. J. Jing, Y. Hou, Y. Luo, L. Chen, L. Ma, Y. Lin, K. H. Li, and Z. Chu, "Chip-scale *in situ* salinity sensing based on a monolithic optoelectronic chip," ACS Sens. **7**, 849 (2022).
185. R. McClintock, K. Mayes, A. Yasan, D. Shiell, P. Kung, and M. Razeghi, "320×256 solar-blind focal plane arrays based on $Al_xGa_{1-x}N$," Appl. Phys. Lett. **86**, 011117 (2004).
186. Y. Luo, D. Wang, Y. Kang, X. Liu, S. Fang, M. H. Memon, H. Yu, H. Zhang, D. Luo, X. Sun, B. S. Ooi, C. Gong, Z. Xu, and H. Sun, "Demonstration of photoelectrochemical-type photodetectors using seawater as electrolyte for portable and wireless optical communication," Adv. Opt. Mater. **10**, 2102839 (2022).